Design and Implementation of a DC/DC Resonant Converter for Power System Applications

By

Arash Fazel Darbandi

A thesis submitted to the Faculty of Graduate Studies of
The University of Manitoba
in partial fulfillment of the requirements for the degree of
Master of Science

Department of Electrical and Computer Engineering
Faculty of Engineering
University of Manitoba
Winnipeg, Manitoba

Abstract

In modern power system, the energy conversion includes a large number of the energy processors, and demands high quality, small, lightweight, reliable and efficient power procedures. The existing linear power regulators can only handle low power levels and demonstrate a low efficiency in the power processing. Pulse-width modulated (PWM) converters demonstrate high turn on and turn off losses, and increase in the electromagnetic interference (EMI). Resonant power conversion becomes more suitable in the renewable energy and energy harvesting applications. Since the resonant conversion requires operating in high frequency, the electrical components such as transformers, filter inductors and capacitors become much smaller and lighter. This can result in reducing size and cost. In addition, use of soft switching technique in the resonant conversion reduced the switching losses and EMI level.

In this research project, a DC/DC resonant converter has been designed and modelled in PSCAD/EMTDC. The functionality of DC/DC resonant converter is validated in a hardware implementation of the small scale DC system.

Acknowledgments

I would like to thank my advisor Dr. Shaahin Filizadeh for providing me with technical help and overall guidance with the project. His enthusiasm and inspiration have proved to be extremely encouraging throughout the project.

I am also grateful for the help from Mr. Erwin Dirks in ordering and assembling parts as well as his technical guidance throughout the project.

I take this opportunity to express my gratitude to Manitoba HVDC Research Centre for their valuable comments and suggestions towards progress of the research.

Of course no one could survive university life without help and support of family and friends. Thanks for all their support in the past two years. Without the combined effort of these people, this project could not have been completed.

.

Dedication

To my beloved parents for their support and courage over the years.

Table of Contents

List of Tables

List of Figures

List of Symbols

A:	Ampere – a unit of electrical current
AC:	Alternating Current – a type of electric current
C:	Capacitor
CPU:	Central Processing Unit
DC:	Direct Current – the unidirectional flow of electric charge
EMI:	Electromagnetic Interface
EMTDC:	Electromagnetic Transients including DC
F:	Farad – a unit of capacitance
GB:	Gigabyte – a unit of digital information in computing
H:	Henry – a unit of inductance
Hz:	Hertz – a unit of frequency
IGBT:	Insulated Gate Bipolar Transistor
KCL:	Kirchhoff's Current Law
KVL:	Kirchhoff's Voltage Law
L:	Inductor
Ohm (Ω):	Ohm – a unit of electrical resistance
PI:	Proportional Integral
PSCAD:	Power System Computer Aided Design
PWM:	Pulse Width Modulation

R:	Resistor
rad:	Radian – a unit of angular measurement
RAM:	Random Access Memory
rpm:	Revolutions per minute – a unit of frequency of rotation
RTDS:	Real-Time Digital Simulator
SW:	Switch
V:	Volt – a unit of electromotive force
VSC:	Voltage Source Converter
W:	Watt – a unit of electric power
ZCS:	Zero Current Switching
ZVS:	Zero Voltage Switching

Chapter 1

Introduction

Conventional electrical power system consists of loads, generations, transmission and distribution systems. The conventional generation plants are driven by some mechanical power source such as hydraulic turbine, steam turbine, gas turbine and etc. while the electrical transmission lines carry electricity at high voltages over long distances to communities [1]. Alternative renewable energy such as wind, solar and battery are increasingly recognized as a technology that will be essential component of the future electrical energy grid. Additionally, renewable energy becomes a new emerging market when every nation in the world seeks to replace their polluting power generating assets into renewable power.

Efficient energy production and storage will play a key role in helping to manage the fluctuations and intermittency issues of renewable energy in the electrical grid [2]. Renewable energy systems cannot directly be connected into the existing grid because the energy generated by the renewable energy is mostly in form of DC such as battery or

solar energy. To overcome this issue and increase the possibility of integrating renewable energy to the grid, power electronic devices need to be implemented into the system. Power electronic technology provides more flexibility in terms of energy conversion and control and has shown a rapid growth in the past two decades in modern power system [3]. The field of power electronics consists of the electrical power using electronic devices. Power electronic devices are versatile and capable of converting AC to AC, AC to DC, DC to AC and DC to DC by having a larger or smaller magnitude or frequency. The conversion phenomenon can be achieved by receiving the raw input power and converting into the conditioned output power specified by the control system [4].

This chapter discusses the energy conversion using resonant circuits and how this phenomenon can be integrated to improve the performance of DC/DC energy conversion. The main focus of this thesis is to design and implement a DC/DC resonant converter for power system applications.

1.1 Motivation and Problem Statement

Energy conversion includes a large number of the energy processors. Even though resonant power conversion is the most suitable approach in the renewable energy and energy harvesting technologies, it has not been used widely in power system because high frequency inductors and transformers with high power rating are expensive and may not be available as off the shelf components; also it requires a complex control system [5-22]. The past two decades have witnessed a revolution in the growth of power electronic technologies. Improvements in this area have led to a smaller, more efficient, lighter, less expensive, and more reliable DC and AC energy converters [3]. Modern electronic

systems require high quality, small, lightweight, reliable and efficient power conversion [21-28]. Linear power regulators are suited for low power levels, typically below 20W, and have a very low efficiency and low power density because they require frequency as low as 50 or 60Hz, line transformers and filters [26]. The transformers, filter inductors, and capacitors size can be reduced by increasing the operating frequency. In addition, the dynamic characteristics of converters improve by increasing operating frequency [26]. The bandwidth of a control loop is usually determined by the corner frequency of the output filter. Therefore, operating at high frequencies allows for reaching a faster dynamic response to quick changes in the load current and/or the input voltage [3].

Pulse-width modulated (PWM) converters are well described in the literature and are still widely used in low and medium power applications [21-27]. However, the PWM waveforms increase the turn on and turn off switching losses that can limit the operating frequency. Moreover, the PWM waveforms can increase the potential for electromagnetic interference (EMI). The incapability of PWM converters to operate with less power efficiency at very high frequencies forces a limit on size of reactive components of the converter and on power density [21-27]. Kazimierczuk [28] searched for the converters capable of operating at higher frequencies, and develop the converter topologies that generate either a sinusoidal current or a sinusoidal voltage waveform, and reduce the switching losses significantly [5-22]. Erickson [4] stated design issues encountered in a variety of products can be solved using the unique capabilities of resonant technology. Information on resonant power technologies is spread throughout many different technical journals, conference proceedings and application notes. In many resonant

DC/DC converters, the switches operate under soft-switching techniques which can reduce the switching losses and EMI levels [24].

1.2 Purpose and Objective

In order to address the issues discussed in the previous section, this thesis investigates the functionality and feasibility of resonant DC/DC conversion in the power system applications. In particular the following items are addressed:

- An investigation of how the resonant DC/DC conversion operates.
- The modelling, design and PSCAD/EMTDC transient simulation of the DC/DC resonant converter.
- The generalized state space averaging modeling of the DC/DC resonant converter.
- The construction of the DC/DC resonant converter.
- Experimentation and analysis of bidirectional operation of the DC/DC resonant converter.
- Experimentation and analysis of functionality of the DC/DC resonant converter with VSC and AC system.

1.3 Thesis Organization

The contents of thesis are organized in the following manner. Chapter 2 provides a deep insight to the theoretical background of DC/DC resonant converters. An in-depth analysis design and simulation of the DC/DC resonant converters are presented in Chapter 3. Chapter 4 provides an investigation into the generalized state space averaging method and verifies the computational efficiency of this approach. Chapter 5 presents the

results of the tests conducted on the DC/DC resonant converter to confirm the functionality and feasibility of the design system. Chapter 6 presents the conclusions and contributions of this research work. In addition, the possible future works based on the outcomes of the research are discussed.

Chapter 2

Principles of Resonant DC/DC Converters

The use of a resonant circuit with an appropriately selected quality factor allows power electronic designers to generate a sinusoidal voltage or current waveform at high frequencies. This topology is often called a DC/DC resonant converter [3]. The resonance circuit generates voltage and current waveforms with zero crossings, which can be useful to improve switching losses. Additionally, soft switching techniques have been used to reduce the switching losses and electromagnetic interference (EMI) levels generated by operation at high frequencies [3]. This chapter contains background information and theory on different resonant circuit topologies, DC/DC conversion with resonance, resonant converter modes of operation, and control approaches. It also presents basic simulation results of a designed DC/DC resonant converter to demonstrate its underlying principles of operation.

2.1 Theory of Resonant Circuits

A resonant converter is essentially based on a second-order RLC circuit. This second order system can be configured in either series or parallel. Figure 2.1 depicts the series and parallel resonant circuits. This section discusses the behavior of each configuration in both time and frequency domains as well as their applications. It also discusses how the eigenvalues or natural frequencies of each configuration depend on variations of the load and the frequency.

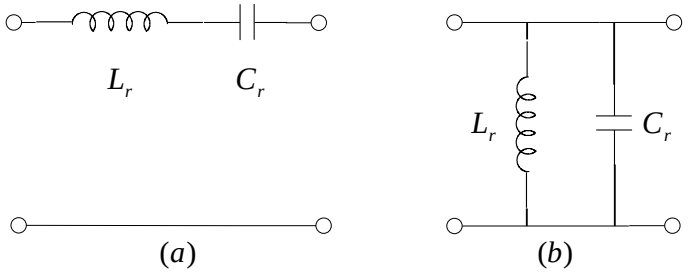

Figure 2.1: (a) A series resonant configuration, (b) A parallel resonant configuration

2.1.1 The Time Domain Response

Figure 2.2 shows the switched series RLC network where, L_r, C_r and R_{load} are resonant tank inductor, capacitor and the equivalent load resistance, respectively.

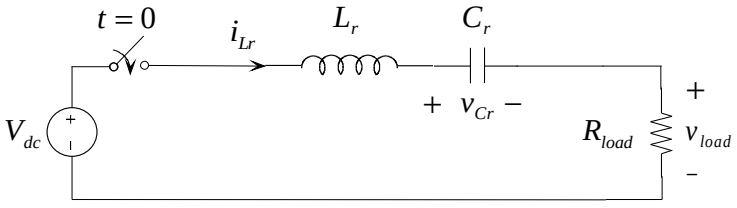

Figure 2.2: The switched series RLC network

By applying KVL and KCL and assuming initial conditions $i_{Lr}(0) = 0$ and $v_C(0) = V_{C0}$, the following equations can be developed for $t > 0$.

$$i_{Lr} = C_r \frac{dv_{Cr}}{dt} \tag{2.1}$$

$$V_{dc} = v_{Rload} + v_{Lr} + v_{Cr} \tag{2.2}$$

$$\frac{d^2 v_{Cr}}{dt^2} + \frac{R_{load}}{L_r}\frac{dv_{Cr}}{dt} + \frac{1}{L_r C_r} v_{Cr} = \frac{V_{dc}}{L_r C_r} \tag{2.3}$$

Defining $\alpha = \frac{R_{load}}{2L_r}$ as the damping coefficient, and $\omega_r = \sqrt{\frac{1}{L_r C_r}}$ as the resonant frequency, one can re-write (2.3) as follows.

$$\frac{d^2 v_C}{dt^2} + 2\alpha\frac{dv_C}{dt} + \omega_r^2 v_C = \omega_r^2 V_{dc} \tag{2.4}$$

This differential equation has natural frequencies, s_1 and s_2, at:

$$s_{1,2} = -\alpha \pm \sqrt{\alpha^2 - \omega_r^2} \tag{2.5}$$

The complete solution to (2.4) is,

$$v_{Cr}(t) = (V_{C0} - V_{dc}) \cdot e^{-\alpha t}\left(\sqrt{1 + \left(\frac{\alpha}{\omega_d}\right)^2}\cos(\omega_d t + \phi)\right) + V_{dc} \tag{2.6}$$

where,

$$\omega_d = \sqrt{\omega_r^2 - \alpha^2} \tag{2.7}$$

$$\phi = \tan^{-1}\left(\frac{\alpha}{\omega_d}\right) \tag{2.8}$$

The damping coefficient, α, linearly depends on the load resistance. As a result, the natural frequencies of the series switched resonant circuit may vary and generate

different response at the output. Figure 2.3 presents the root locus characteristic of the natural frequency as the load resistance varies.

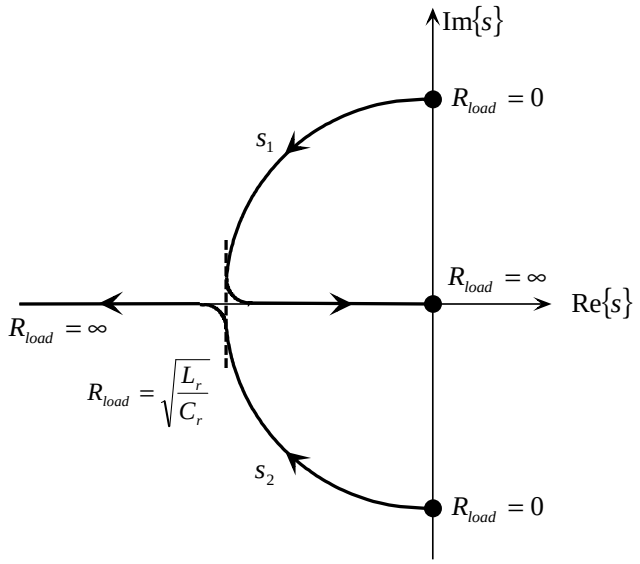

Figure 2.3: The root locus characteristic of the natural frequencies as the load varies

At short circuit condition, $R_{load}=0$, the damping coefficient, α, becomes zero. Therefore, (2.6) can be expressed as follow,

$$v_{Cr}(t) = \left(V_{C0} - V_{dc}\right) \cdot \cos\left(\omega_r t\right) + V_{dc} \tag{2.9}$$

The capacitor voltage oscillates around V_{dc} at the resonant frequency of ω_r as both poles are located on the imaginary axis with zero real part. However, at no load condition, i.e. $R_{load}=\infty$, the damping coefficient, α, becomes infinity. Therefore, (2.6) can be expressed as (2.10) where the capacitor voltage becomes constant DC voltage at V_{dc} .

$$v_{Cr}(t) = V_{dc} \tag{2.10}$$

Figure 2.4 shows the switched parallel RLC network where L_r, C_r and R_{load} are the resonant tank inductor, capacitor and the equivalent load resistance, respectively.

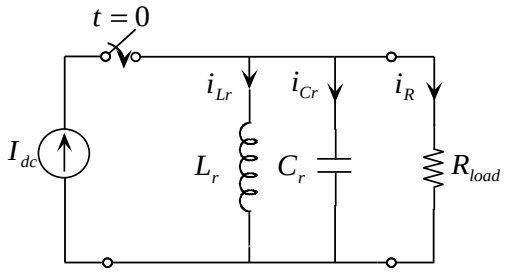

Figure 2.4: The switched parallel RLC network

A similar approach can be applied to determine the second order differential equation of the circuit shown in Figure 2.4.

$$\frac{d^2 i_{Lr}}{dt^2} + \frac{1}{R_{load} L_r}\frac{di_{Lr}}{dt} + \frac{1}{L_r C_r} i_{Lr} = \frac{I_{dc}}{L_r C_r} \tag{2.11}$$

Since (2.3) and (2.11) are similar, the complete solution to (2.11) can be obtained as,

$$i_{Lr}(t) = (I_{L0} - I_{dc}) \cdot e^{-\alpha t}\left(\sqrt{1+\left(\frac{\alpha}{\omega_d}\right)^2}\cos(\omega_d t + \phi)\right) + I_{dc} \tag{2.12}$$

where ω_d and ϕ are defined in (2.7) and (2.8), respectively.

As a result, the natural frequencies of the parallel switched resonant circuit can vary and generate different response at the output and presents the same root locus characteristic as the series resonant network. The only difference is when there is short circuit, i.e. $R_{load}=0$, the damping coefficient, α, becomes zero. Therefore, (2.12) can be expressed as follow,

$$i_{Lr}(t) = (I_{L0} - I_{dc}) \cdot \cos(\omega_r t) + I_{dc} \tag{2.13}$$

The inductor current will oscillate around I_{dc} at the resonant frequency of ω_r as both poles are located on the imaginary axis with zero real part. However, at no load condition, $R_{load}=\infty$, the damping coefficient, α, becomes infinity. Therefore, (2.13) can be expressed as (2.14) where the inductor current becomes constant DC current at I_{dc}.

$$i_{Lr}(t)=I_{dc} \tag{2.14}$$

A series-parallel resonant network is the combination of both series and parallel resonant circuit, so it can behave similarly to both. Figure 2.5 shows the switched series-parallel resonant network where L_r , C_r and C_p are the inductor, the series capacitor and the parallel capacitor of the resonant tank, respectively.

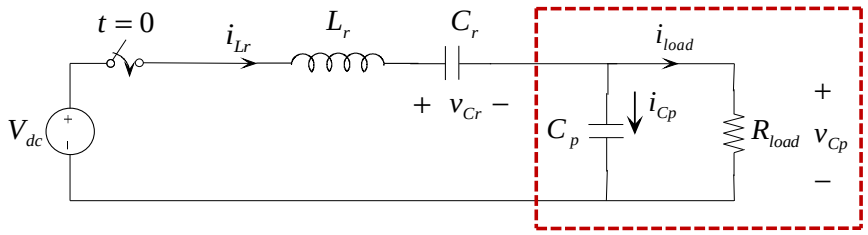

Figure 2.5: The switched series-parallel RLC network

The parallel capacitor C_p and R_{load} combination can be converted into an equivalent series C_s and R_s circuit using (2.15) and (2.16) transformation [29].

$$C_s = C_p \frac{1+A^2}{A^2} \tag{2.15}$$

$$R_s = R_{load} \frac{1}{1+A^2} \tag{2.16}$$

$$A=\omega \cdot C_p R_{load} \tag{2.17}$$

Figure 2.6 depicts the simplified equivalent circuit where

$$C_{eq} = \frac{C_r C_s}{C_r + C_s} \tag{2.18}$$

$$R_{eq} = R_s \tag{2.19}$$

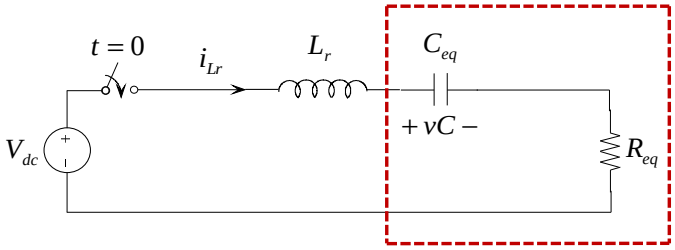

Figure 2.6: The simplified equivalent circuit

For this new configuration, both damping coefficient, α, and resonant frequency, ω_r, depend on R_{load} and the frequency of operation. Figure 2.7 depicts the root locus characteristic of the natural frequencies as the resistance load and operating frequency vary.

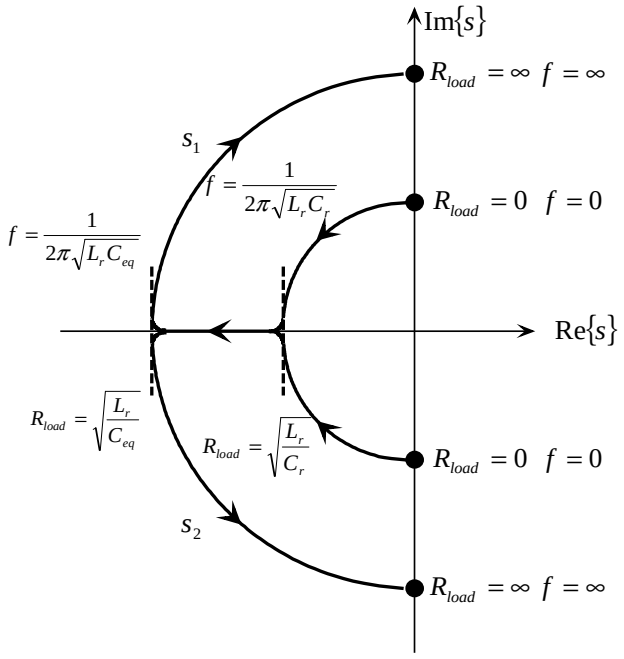

Figure 2.7: The root locus characteristic of the natural frequencies as the load and frequency vary

As a result, the natural frequencies of the series-parallel switched resonant circuit can vary and generate different response at the output and present the same root locus characteristic as the series resonant network. The only difference is when there is short circuit, $R_{load}=0$, and at no load condition, $R_{load}=\infty$, the damping coefficient, α, becomes zero. Therefore, (2.12) can be expressed as follow,

$$v_C(t) = (V_{C0} - V_{dc}) \cdot \cos(\omega_r \cdot t) + V_{dc} \tag{2.20}$$

The capacitor voltage oscillates around V_{dc} at the resonant frequency of ω_r as both poles are located on the imaginary axis with zero real part. However, at $R_{load} = \sqrt{\frac{L_r}{C_r}}$ and $\omega = \frac{1}{\sqrt{L_r C_r}}$, the damping coefficient, α, becomes $\frac{\omega}{2}$. Because the resonant network is operating at high frequencies, $e^{-\alpha t}$ factor converges to zero. Therefore, (2.6) can be expressed as (2.21) where the capacitor voltage becomes constant DC voltage at V_{dc}.

$$v_C(t) = V_{dc} \tag{2.21}$$

2.1.2 The Frequency Domain Response of the Series-Parallel Resonant Circuit

Figure 2.8 presents a square wave voltage waveform. By applying Fourier analysis, given in (2.22), the harmonic components of the given square wave can be extracted as given in (2.23).

$$C_n = \frac{1}{T}\int_T x(t)\cdot e^{-jn\frac{2\pi}{T}t}\,dt \tag{2.22}$$

$$|C_n| = \begin{cases} 0 & n:even \\ \dfrac{2\cdot V_{dc}}{n\pi} & n:odd \end{cases} \tag{2.23}$$

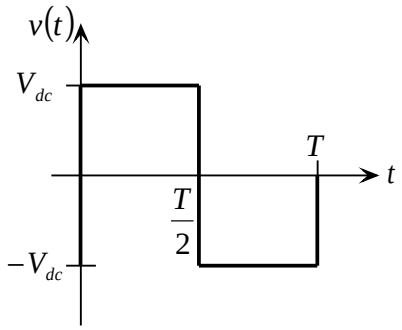

Figure 2.8: A square wave voltage waveform

Figure 2.9 shows the fundamental and the fundamental plus the 3rd harmonic components of the square wave. Every square-wave waveform has a fundamental frequency sinusoidal component as specified by (2.23), and their embedded sine-wave can be extracted using a low pass filter. Therefore, a passive resonant low pass filter can be designed in such a way to generate a good quality sinusoidal waveform from a given square wave.

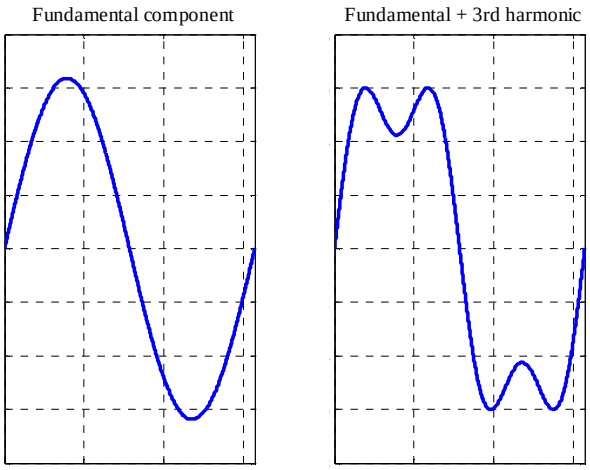

Figure 2.9: The fundamental and the fundamental plus the 3rd harmonic of the square wave

The admittance of the RLC circuit shown in Figure 2.5 as a function of complex frequency $s = j\omega$ is:

$$Y(s) = \frac{\frac{1}{L_r}s^2 + \frac{1}{R_{load}C_p}s}{s^3 + \frac{1}{R_{load}C_p}s^2 + \frac{C_r + C_p}{L_r C_r C_p}s + \frac{1}{R_{load}L_r C_r C_p}} \tag{2.24}$$

Table 2.1 summarizes the calculated parameters of a 5kW, 1000V resonant RLC circuit shown in Figure 2.5 as designed in Appendix B.

Table 2.1: The selected parameters for RLC circuit shown in Figure 2.5

L_r	$40\,\mu H$
C_r	$1.2\,\mu F$
C_p	$1.2\,\mu F$
R_{load}	$250\ \Omega$

Figure 2.10 depicts the frequency response characteristic of the resonant circuit shown in Figure 2.5. The resonant frequency of the designed low pass filter is 32.5kHz. This means at resonant frequency, the resonant circuit acts as a short circuit, therefore, the voltage component with a 32.5kHz across the load is equal to the source voltage.

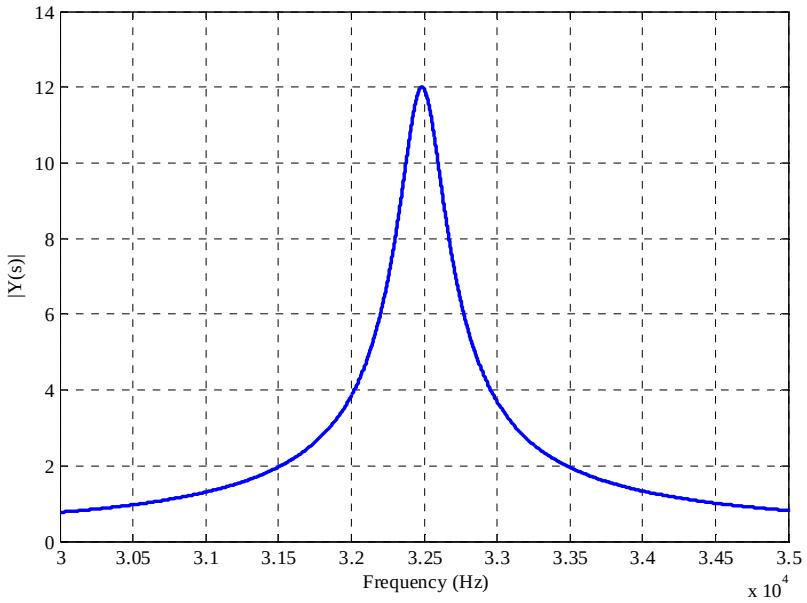

Figure 2.10: Frequency domain response of the RLC circuit shown in Figure 2.5

The quality factor, *Q*, defines the ratio of the energy stored in the resonator to the energy supplied by a generator per cycle [23].

$$Q = \frac{2\pi \times Peak\ Stored\ Energy}{Energy\ Dissipated\ Per\ Cycle} = \frac{f_0}{\Delta f} \qquad (2.25)$$

As shown in Figure 2.10, the quality factor of the filter is high enough to attenuate the 3rd, and 5th harmonic components of the input square wave at 25.3kHz as shown in Figure 2.11.

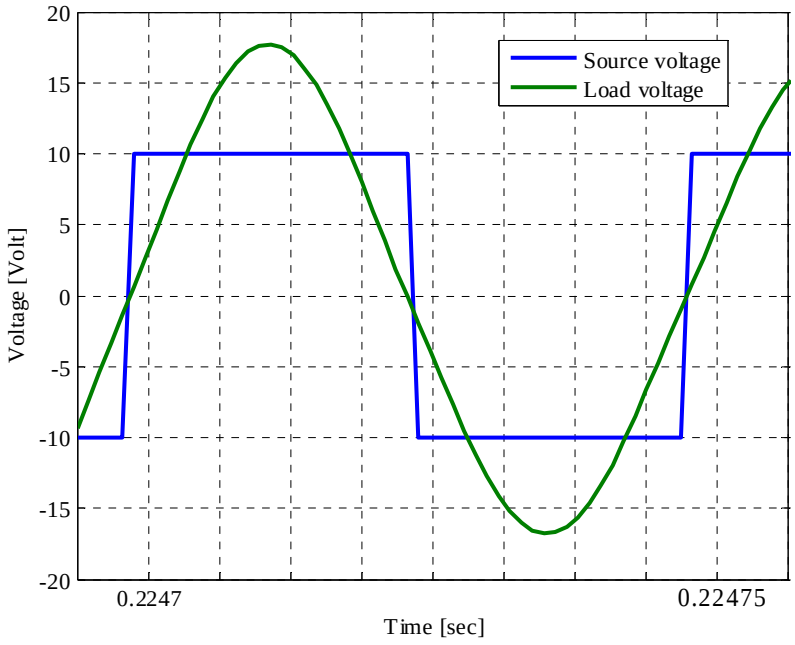

Figure 2.11: The output voltage at 25.3kHz after removing the odd harmonics by passing through the resonant circuit

2.2 DC/DC Conversion with Resonance

The main purpose of using DC/DC conversion is to generate controllable DC voltages from a fixed DC source. Mohan et al [24] discussed many approaches, which can be used to generate a controllable DC voltage using a fixed DC source. As discussed in section 2.1, it is possible to generate a purely sinusoidal waveform from a resonant circuit. The DC/DC resonant converter uses this capability of the resonant filters to generate a controllable DC voltage. A resonant DC/DC converter can be obtained by cascading an inverter and a rectifier as shown in Figure 2.12. A high frequency transformer can also be used if isolation is required.

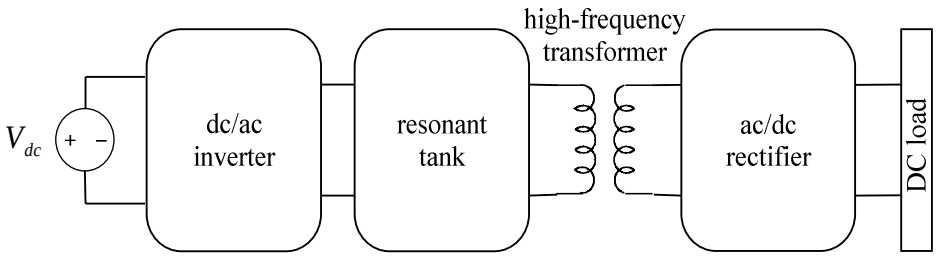

Figure 2.12: A resonant DC/DC converter block diagram

A square wave voltage can be generated by using either half-bridge or a full-bridge converter. Figure 2.13 shows the configuration scheme of both half and full bridge converter.

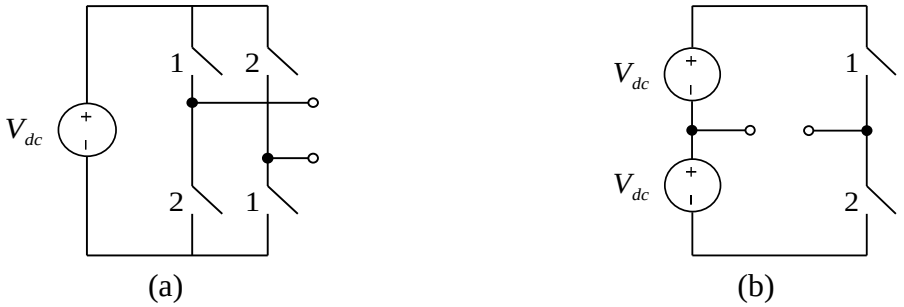

Figure 2.13: (a) The full-bridge configuration scheme (b) The half-bridge configuration scheme

The disadvantages of the half-bridge configuration are that two DC sources are required and each switch is stressed by a voltage or current equal to $2 \cdot V_{dc}$. However, only one DC source is required in full-bridge configuration and reduces the stress of switches [23]. Therefore, the full-bridge topology was used in this project.

The purpose of DC/AC inverter is to generate a square wave voltage by using a full-bridge inverter from a fixed voltage source. Figure 2.14 (a) and (b) show a full-bridge configuration scheme and the output voltage generated by the inverter, respectively. The

output voltage remains at $+V_{dc}$ when the switches 1 are on and 2 are off. The output voltage becomes $-V_{dc}$ once the switches 2 are on and 1 are off.

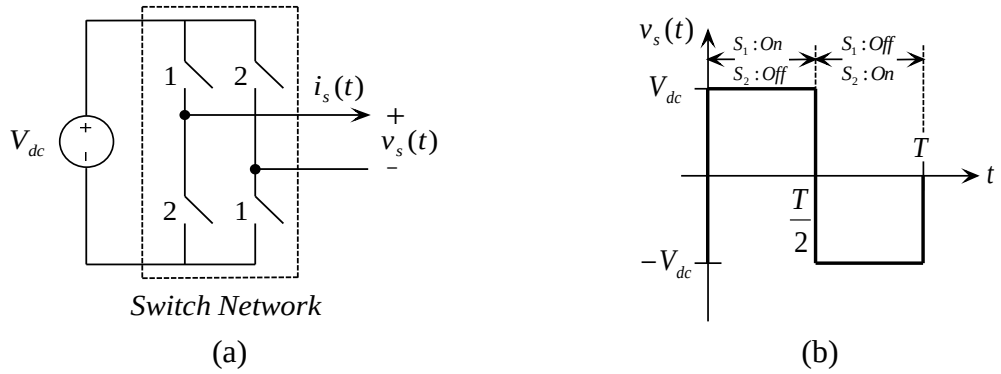

Figure 2.14: (a) The full-bridge inverter configuration scheme (b) The output voltage

The generated square wave voltage will excite the resonant circuit. As discussed in section 2.1, the resonant circuit converts the square wave input voltage into a sinusoidal voltage source by removing the additional harmonic components of square wave.

The generated sinusoidal waveform can be rectified as shown in Figure 2.15. The rectified waveform contains a DC component. A fairly large capacitor is usually employed to remove the DC component and to provide energy for the load.

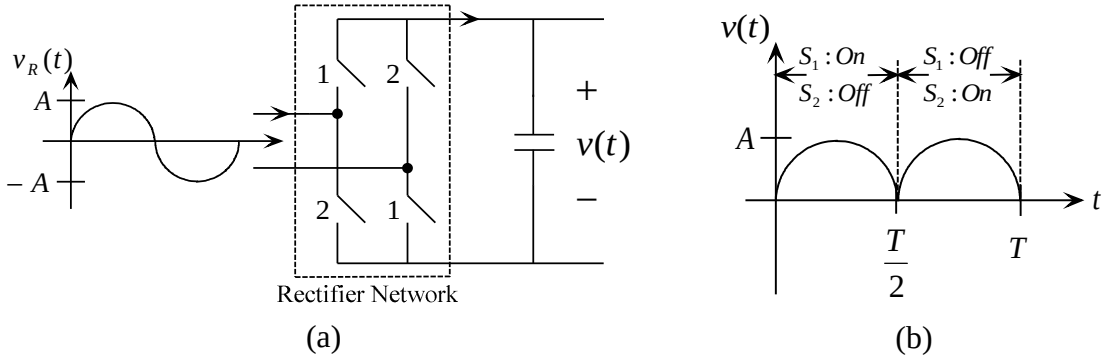

Figure 2.15: (a) The full-bridge rectifier configuration scheme (b) The output voltage

This representation approach is suitable from an analytical point of view. Chapter 4 will discuss the analytical representation of DC/DC resonant converter.

It is important to connect a compatible inverter and rectifier in order to develop a DC/DC resonant converter. For instance, if the rectifier requires an input voltage source, i.e. voltage-driven rectifier [3], an inverter whose output behaves as a voltage source needs to be connected. As explained in 2.1.1, a parallel resonant circuit has this capability. Similarly, a series resonant circuit can drive a current source for a current driven rectifier. A series-parallel resonant circuit demonstrates an intermediate characteristic. If an isolation transformer is used, the parallel capacitor can also be placed on the secondary side. This way the transformer leakage inductance can be included in the resonant circuit inductor. Therefore, it reduces the size, cost and volume of the resonant tank inductance.

Resonant DC/DC converters have the feature that their switching frequency equals the fundamental AC frequency of the intermediate AC. As stated before, the full-bridge inverter creates a square wave AC waveform from the DC source, and the resonant filter removes the undesired harmonic components from the input waveforms. Subsequently, since the difference in frequency between the fundamental component and the 3^{rd} harmonic, the lowest harmonic of the square wave, is relatively small, a resonant circuit can be used to approximate the switching frequency rather than a low pass filter. If the resonant filter has a high quality factor, it can provide sufficient controllability. Chapter 4 will discuss more of resonant converters' control strategies. Capability of transferring energy in both directions demonstrates another advantage of resonant converter.

The energy loss of a switching device can be calculated as follows [23]:

$$E_{loss} = \int_{0}^{t_{on,off}} v_{sw} i_{sw} dt \tag{2.26}$$

where $t_{on,off}$ is the time it takes the semiconductor device to turn on or off, i.e. the rise or fall time of its current and/or voltage. A resonant converter can be designed such that one of the switch variables remains close to zero during its switching period. As a result, it causes less switching losses in the semiconductor devices. This is one of the advantages of the resonant converters. However, it results in higher stress on semiconductor switches and may increase the conduction losses of the device [23].

2.3 Control Modes of Resonant Converters

Resonant converters usually control the direction of power by changing the switching frequency [23]. Therefore, resonant converters can only be used if the exact frequency of the AC system does not matter or when the DC voltage can be varied to control power.

If the switching frequency is slightly higher or lower than the resonant frequency, the resonant tank filter behaves similar to a small inductor or a large capacitor. As a result, the voltage across the load resistor changes accordingly. However, if the resonant tank filter has a higher quality factor, the magnitude of the voltage changes drastically with any small variation of frequency. Changing the frequency is one approach to control the output voltage; however, it has some disadvantages. If the switching frequency is lower than the resonant frequency, it would be possible for the third harmonic of the square wave to be at the cut off frequency of the resonant tank filter. As a result, the third harmonic current would flow into the load. This can be more critical if the resonant tank quality factor is low and the admittance curve of the resonant tank is broad. This problem

forces a lower limit on the switching frequency and/or the quality factor of the resonant tank filter. Moreover, when the switching frequency is higher than the resonant frequency, the harmonic components of the square wave are always filtered out, but switching devices have an upper limit to their switching frequency, which adds to their limitations [23].

As discussed in section 2.2, a full-bridge inverter is capable of generating a square waveform. Now, if the switches turn on and off with delay, the output square wave voltage will contain a phase shift as shown in Figure 2.16.

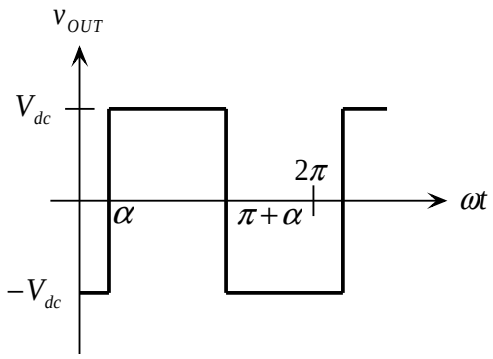

Figure 2.16: The output voltage waveform of a full bridge inverter with phase shift

By applying Fourier analysis, given in (2.22) and (2.23), the fundamental component of the periodic waveform shown in Figure 2.16 is determined as given in (2.27).

$$V_{OUT} = \frac{4V_{dc}}{\pi} = 2 \cdot |C_1| \tag{2.27}$$

If the resonant frequency and switching frequency remain the same, the fundamental component of input waveform will appear across the resistive load. Therefore, the output power can be controlled by varying α from 0 to 90° while maintaining the switching frequency equal to the resonant frequency. This control approach provides a broad range

of control by keeping the switching frequency constant. The advantage of phase shift control is that a high quality factor resonant filter can be used to remove switching frequency noise from sensitive equipment external to the power circuit [23].

2.4 Elementary Simulation Results

This section presents the elementary simulation results to demonstrate the basic operation of DC/DC resonant converter. Figure 2.17 depicts a simple full-bridge inverter connected to a resistive load through a series-parallel resonant circuit designed in Appendix B.

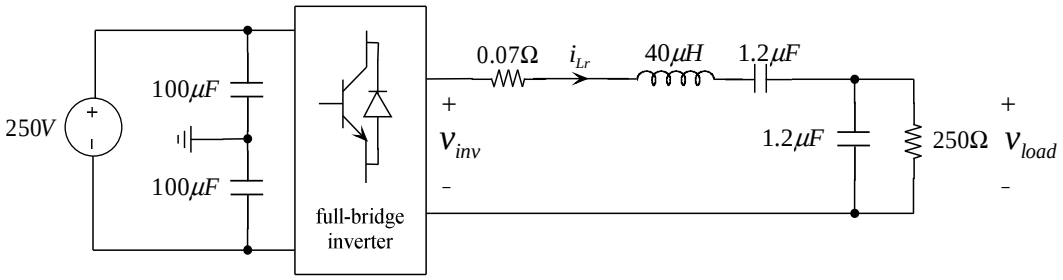

Figure 2.17: A full-bridge inverter connected to a resistive load through a series-parallel resonant circuit

Figure 2.18 presents the results of the circuit developed in Figure 2.17. As expected the output voltage of inverter is a square wave with magnitude of 250V while the load voltage and current are sinusoidal waveforms with the same fundamental frequency of 25.3kHz. Resonant circuit current clearly demonstrates the charge and discharge duration of resonant tank inductor. The inductor needs to be discharged completely in order to reverse the direction of current. Since the direction of inductor current cannot change

instantaneously, a small dip is created where the switching transition occurs. This can be mitigated by soft switching techniques described in Chapter 3.

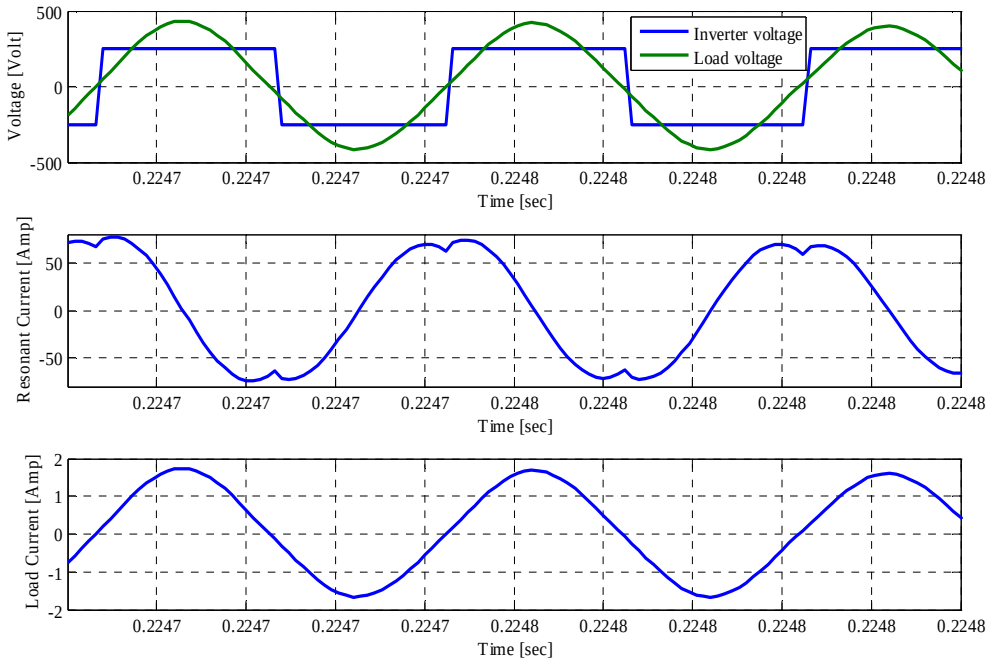

Figure 2.18: The voltage, resonant current (i_{Lr}) and output current

Figure 2.19 presents a similar circuitry having a full-bridge rectifier connected between the resonant tank and the resistive load.

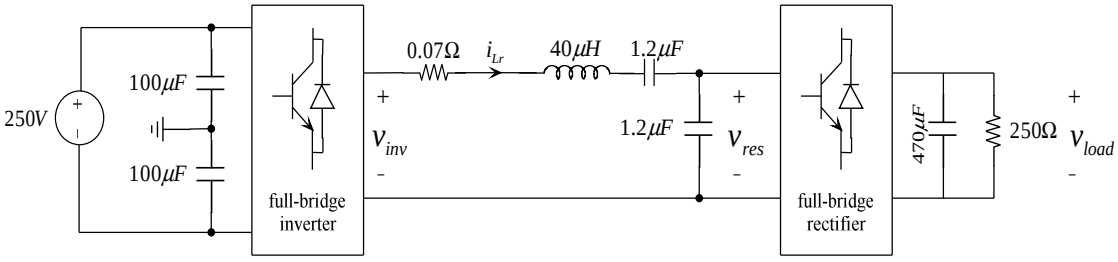

Figure 2.19: A simple DC/DC resonant converter

Figure 2.20 presents the results of the circuit developed in Figure 2.19. As expected the output voltage of inverter and the input voltage of the rectifier are square wave with magnitude of 250V and a delay of 0.18rad with frequency of 25.3kHz. The phase shift is generated by the control system to maintain the load voltage at the desired value 250V. Chapter 3 will discuss the design of a control system in more details. Resonant circuit current clearly demonstrates the charge and discharge duration of resonant tank inductor.

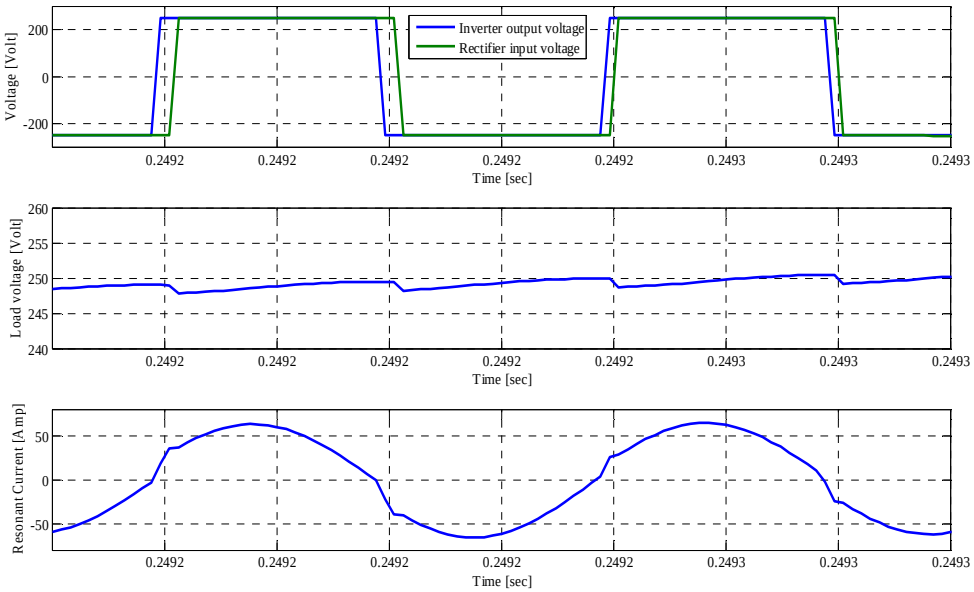

Figure 2.20: The voltage, load voltage, and resonant current (i_{Lr})

Next chapter will discuss the detailed control design, and simulation results of multiple DC/DC resonant converters connected to a grid.

Chapter 3

Modeling and Simulation of DC/DC Resonant Converter

This chapter contains details on modeling DC/DC resonant converters, control system design, and finally presents a number of different case studies to demonstrate the different applications of DC/DC resonant converters. The developed simplified model can be used to conceptualize and construct a more complex system. The system modeling also simplifies the analysis and design of a small scale DC grid.

3.1 Modeling

Chapter 2 presented a general overview of a DC/DC resonant converter. Figure 3.1 depicts the circuit under consideration in this chapter.

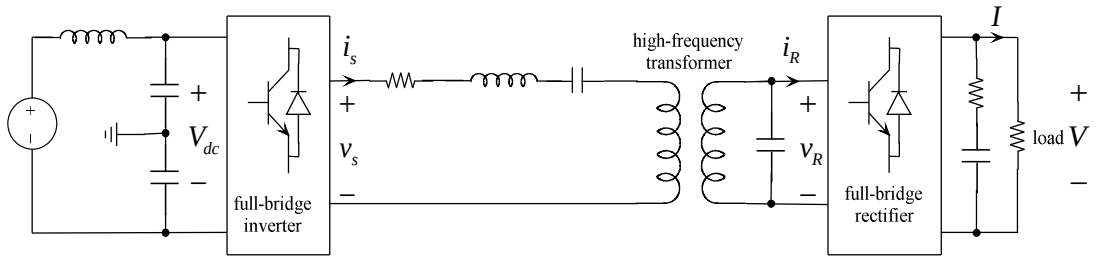

Figure 3.1: The circuit under consideration

The cascaded representation as shown in Figure 3.1, is suitable for analysis and modeling of full-bridge inverter and rectifier. This section provides a detailed modeling of DC/DC resonant converter and compares with the detailed system.

3.1.1 Resonant Inverter Modeling

As discussed in section 2.2, if the quality factor of a resonant circuit is high enough and the switching frequency is close enough to the resonant frequency, a full-bridge inverter is capable of generating either a sinusoidal output current or a sinusoidal output voltage, depending on the resonant circuit topology. Therefore, the entire inverter can be replaced by a sinusoidal current source or a sinusoidal voltage source where the magnitude of the fundamental component of the square wave can be determined (2.23). Therefore, the full-bridge inverter can be modeled as a combination of current and voltage source where the DC component of the output current can be modeled as follows,

$$\langle i_s(t)\rangle_{Ts} = \frac{2}{T_s}\int_0^{Ts/2} I_{s1}\sin(\omega_s\tau)d\tau = \frac{2}{\pi}I_{s1} \qquad (3.1)$$

Figure 3.2 depicts the equivalent circuit diagram of a full-bridge inverter.

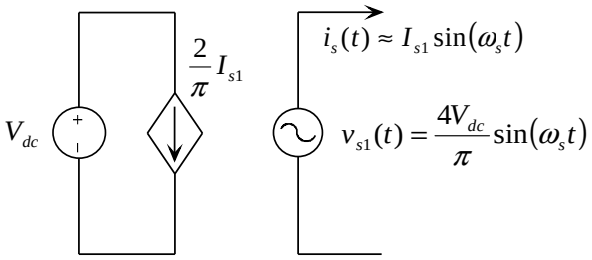

Figure 3.2: The switch network equivalent circuit of a full-bridge inverter [17]

3.1.2 Resonant Rectifier Modeling

The full bridge rectifier and the output filter network are presented in Figure 3.3. The output filter is assumed to be large enough to eliminate the entire ripple passing through the load. As shown in Figure 3.1, when a full-bridge inverter, a resonant circuit and a full-bridge rectifier are cascaded, the input voltage of the rectifier is also a square wave with a zero crossing in phase with the resonant network current where the magnitude of its fundamental component can be determined by (2.23). Therefore, the input of rectifier can be modeled as a sinusoidal voltage source with a phase shift generated by the resonant circuit. The DC load current, however, can be determined as the DC component of the rectifier input current as follows,

$$\left\langle \left| i_R(t) \right| \right\rangle_{Ts} = \frac{2}{T_s} \int_0^{Ts/2} I_{R1} \left| \sin(\omega_s t - \delta) \right| dt = \frac{2}{\pi} I_{R1} \cos\delta \qquad (3.2)$$

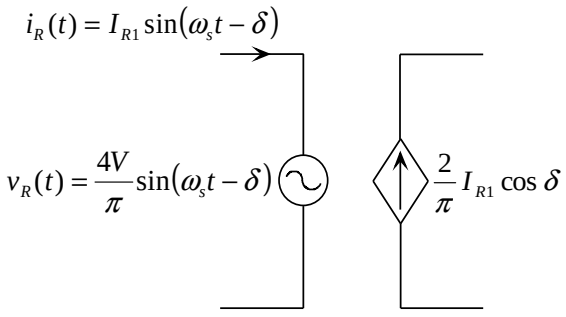

Figure 3.3: The switched network equivalent circuit of a full-bridge rectifier

3.1.3 Resonant Network Modeling

By removing the power electronic components and replacing them by a voltage or current source, the system can be reduced to a linear circuit as shown in Figure 3.4.

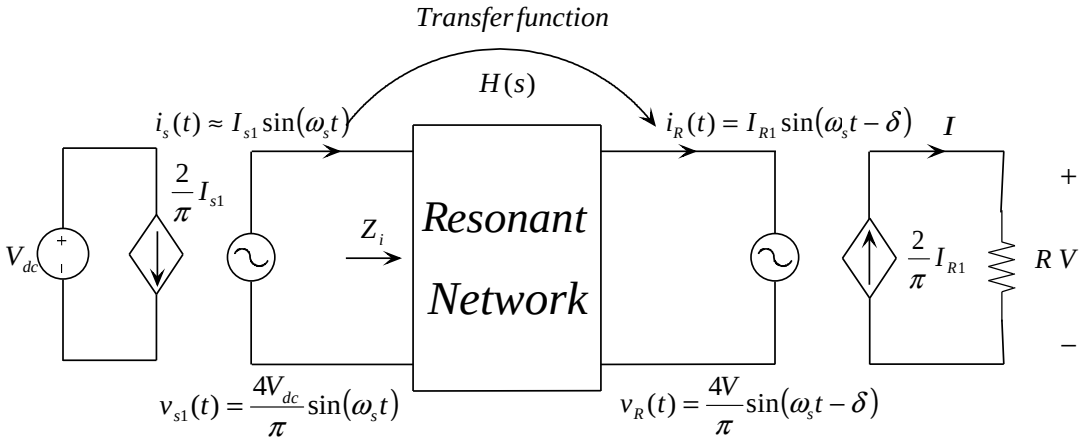

Figure 3.4: The simplified dc/dc resonant converter

The DC/DC resonant converter transfer function is calculated in (3.3) where H(s) is the transfer function of the resonant circuit.

$$M = \frac{V}{V_{dc}} = \left(\frac{V}{I}\right)\cdot\left(\frac{I}{I_{R1}}\right)\cdot\left(\frac{I_{R1}}{V_{R1}}\right)\cdot\left(\frac{V_{R1}}{V_{s1}}\right)\cdot\left(\frac{V_{s1}}{V_{dc}}\right) \tag{3.3}$$

$$M = \frac{V}{V_{dc}} = (R)\cdot\left(\frac{2}{\pi}\right)\cdot\left(\frac{I_{R1}}{V_{R1}}\right)\cdot\left\|H(s)\right\|_{s=j\omega_s}\cdot\left(\frac{4}{\pi}\right) \tag{3.4}$$

3.2 Zero-Current Switching or Zero-Voltage Switching

As explained in Chapter 2 one of the advantages of the resonant converter is the reduced switching losses when the switching happens exactly at the resonant frequency.

At $\omega_s = \omega_r$, the zero crossing of switching current occurs at the same time as switches are changing states. As a result, almost no energy is lost during switches changing states. If the switching frequency occurs below the resonance frequency, the input resonant network current leads the voltage. Therefore, the zero-current switching (ZCS) occurs.

Zero-voltage switching (ZVS) happens when the switching frequency is above the resonance frequency. The resonant network input impedance becomes more inductive. The angle of input impedance becomes negative, which means the input current lags the input voltage. Therefore, the zero crossing of the input voltage occurs before the zero crossing of the current.

Soft switching at the ZVS can be implemented by placing small capacitors across each switching device, or introduce a delay between turn off and turn on of each sequence. The capacitor will be charged and discharged by the current passing through each leg of the full-bridge converter. Consequently, the turn off transition becomes almost lossless because no conduction will occur during the commutation interval. The ZVS demonstrates a low switching loss and the diode stored charge losses and switches output capacitance will be eliminated [17].

Erickson [17] proves that if the resonant network is purely reactive, the boundary between zero-current switching and zero-voltage switching occurs when the load resistance *R* equals to the critical value R_{crit}, given by

$$R_{crit} = \|Z_{o0}\| \sqrt{\frac{-Z_{i\infty}}{Z_{i0}}} \tag{3.5}$$

Figure 3.5 shows the boundary between ZVS and ZCS. The ZVS/ZCS boundary is function of $Z_{i\infty}$ and Z_{i0}. If ZVS occurs at open circuit and at short circuit, then ZVS

occurs for all loads. If ZVS occurs at short circuit, and ZCS occurs at open circuit, then ZVS is obtained at matched load provided that $\|Z_{i\infty}\| > \|Z_{i0}\|$ [14].

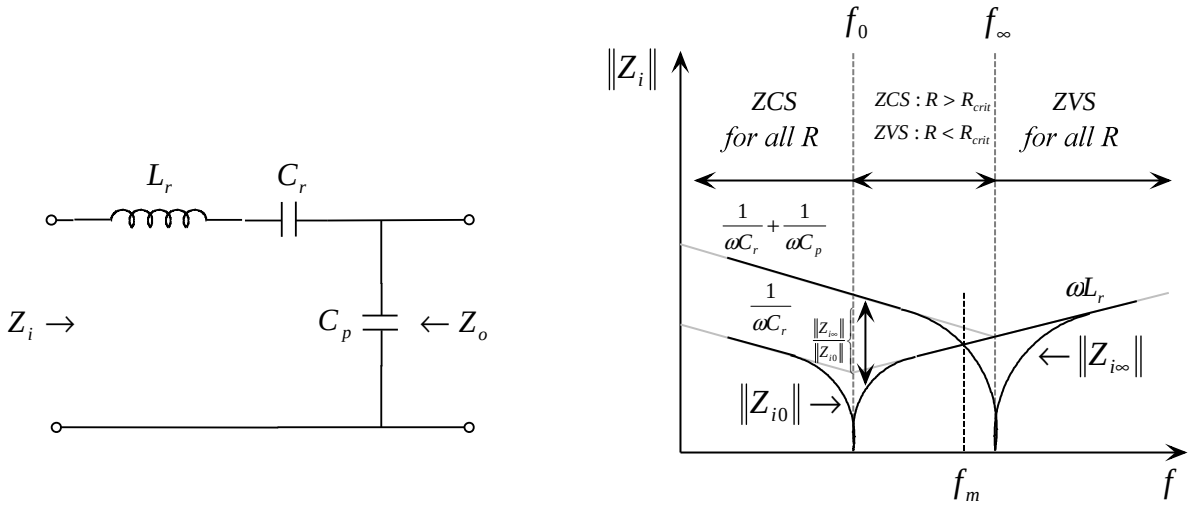

Figure 3.5: The boundary between ZVS and ZCS [17]

ZVS mitigates the switching losses caused by diode recovered charge and switching devices output capacitances. Therefore, the ZVS techniques must be implemented for the applications where the switching losses and EMI needs to be minimized. On the other hand, the ZCS techniques can also reduce the switching losses due to the tail current in IGBTs [17].

3.3 DC/DC Resonant Converter Control System Design

As explained in Chapter 2, the phase shift control approach is the most effective way to control DC/DC resonant converters, and can be obtained by cascading phase controlled full-bridge resonant inverter and rectifiers as shown in Figure 3.1. Figure 3.6 shows the

power flow through the equivalent resonant network. The complex power can be expressed as follows,

$$S = V \cdot I^{*} = P + jQ \tag{3.6}$$

where

$$P = \frac{V^2}{X} \sin\delta \tag{3.7}$$

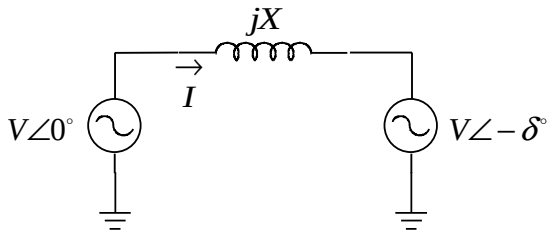

Figure 3.6: The power flow through an equivalent resonant network

Therefore, the amount of power transferred in forward and reverse directions can be controlled by the phase angle. The DC output voltage can also be regulated against load current and line voltage variations by varying the phase shift while maintaining a fixed operating frequency.

State space modeling approach is used next in order to design and study the control system for DC/DC resonant converters.

3.3.1 Analysis of Control Systems in State Space

Since the DC/DC resonant converters are non-linear systems, linearization is necessary in order to design a linear control system. The system equations of Figure 3.1 are developed

and converted into d-q frame. Appendix D explains the d-q modeling of a single phase system. The system state space is determined in Appendix E as follows,

$$\dot{X} = A \cdot X + B \cdot U \tag{3.8}$$

$$Y = C \cdot X \tag{3.9}$$

where,

X is the state vector

Y is the output vector

U is the input or control vector

A is the state matrix

B is the input matrix

C is the output matrix

The stated matrices for a 5kW, 1000V DC/DC resonant converter designed in Appendix B are summarized in Table 3.1.

Table 3.1: The state space matrices for a 5kW, 1000V DC/DC resonant converter

$$A = \begin{bmatrix} -959.2 & -1.53e4 & -3.43e3 & 0 & 0 & 0 \\ 1.53e4 & 959.2 & 0 & -3.43e3 & 0 & 0 \\ 3.05e6 & 0 & -346.8 & -1.6e5 & -1.5e7 & 0 \\ 0 & 3.05e6 & 1.6e5 & -3.9e4 & -1.45e6 & 0 \\ 0 & 0 & 6.4e3 & 596.2 & 0 & -1e4 \\ 0 & 0 & 0 & 0 & 2.12e3 & -8.5 \end{bmatrix} \qquad \lambda = \begin{Bmatrix} -4.2e3 + j3.7e5 \\ -4.2e3 - j3.7e5 \\ -1.47e4 + j9.0e4 \\ -1.47e4 - j9.0e4 \\ -8.5e2 + j7.1e2 \\ -8.5e2 - j7.1e2 \end{Bmatrix}$$

$$R_{load} = 250\,\Omega$$

$$B = \begin{bmatrix} -2.7e6 \\ 0 \\ 0 \\ 0 \\ 0 \\ 0 \end{bmatrix} \qquad C = \begin{bmatrix} 0 & 0 & 0 & 0 & 0 & 1 \end{bmatrix}$$

The eigenvalues of matrix A are the roots of the characteristic equation (3.10).

$$|\lambda I - A| = 0 \tag{3.10}$$

The eigenvalues are determined when load varies from short circuit to open circuit, $R_{load}: 0 \rightarrow \infty$. Figure 3.7 represents the root locus of DC/DC resonant converter under consideration.

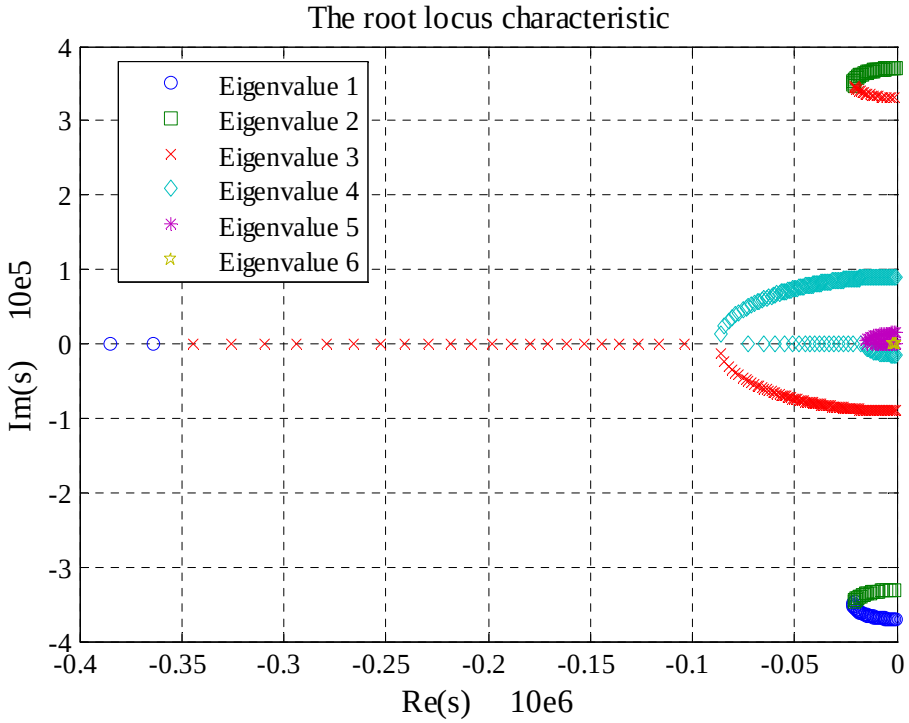

Figure 3.7: The root locus characteristic

All the eigenvalues of the system matrix *A* have negative real part, which demonstrates the stability of the designed system.

A system is completely state controllable if it is possible to drive the system from any initial state $x(t_0)$ to any final state $x(t_1)$ in a finite time duration $t_1 - t_0$ by applying

some input signal $u(t)$ [30]. A system is controllable if the $n \times n$ controllability matrix (3.11) has full rank. Note that a matrix has full rank if its determinant is non-zero.

$$M_C = \begin{bmatrix} B & A \cdot B & A^2 \cdot B & .... & A^{n-1} \cdot B \end{bmatrix} \tag{3.11}$$

The designed system state controllability versus load variation is presented in Figure 3.8. This means the designed system can be driven from any initial state to any final state in finite time duration.

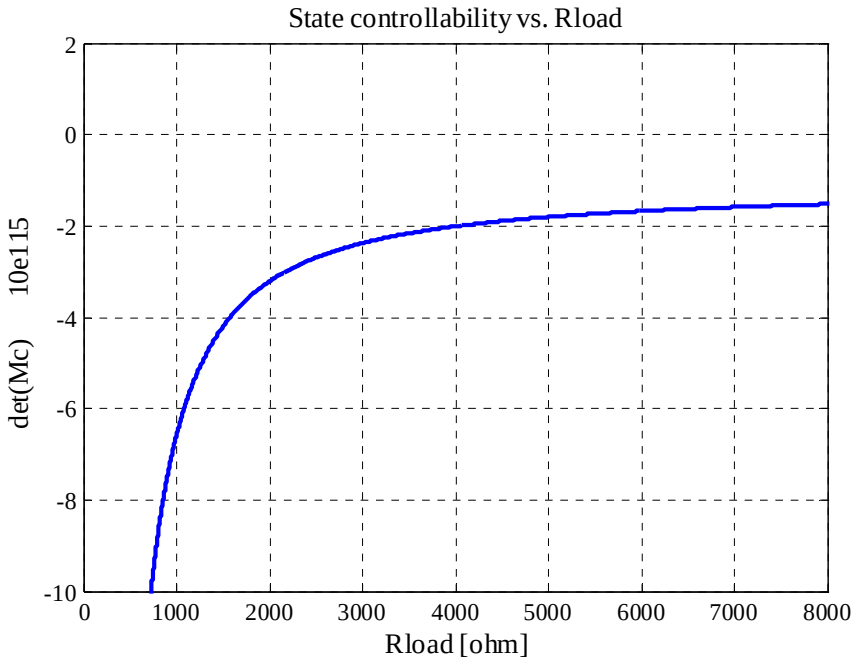

Figure 3.8: The state controllability vs. Rload

Moreover, a system is completely state observable if every state at time t_0 can be determined by observing the system output $y(t)$ for finite time duration $t_0 \le t < t_1$ [30]. A system is observable if the $n \times n$ observability matrix (3.12) has full rank.

$$M_O = \begin{bmatrix} C \\ C \cdot A \\ C \cdot A^2 \\ .... \\ C \cdot A^{n-1} \end{bmatrix} \tag{3.12}$$

The designed system state observability versus load variation is presented in Figure 3.9. This means the designed system output can be observed at time t_0 for finite time duration except when the load is 30Ω. An observer needs to be added to the control system to achieve the observability criteria for all loading conditions.

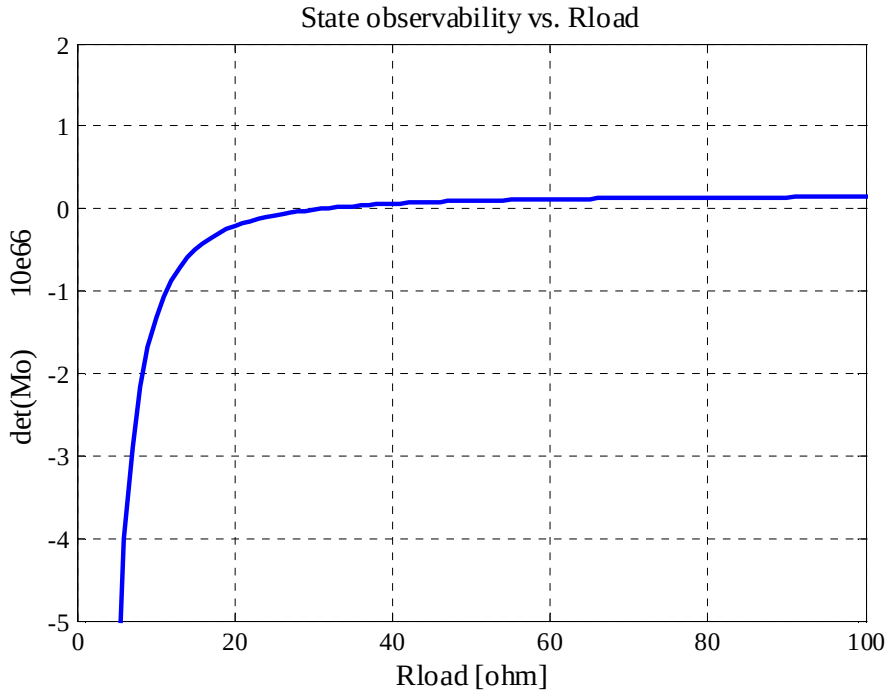

Figure 3.9: The state observability vs. Rload

3.3.2 Design of Control Systems

Figure 3.10 presents the unit step response of DC/DC resonant converter when $R_{load} = 8k\Omega$.

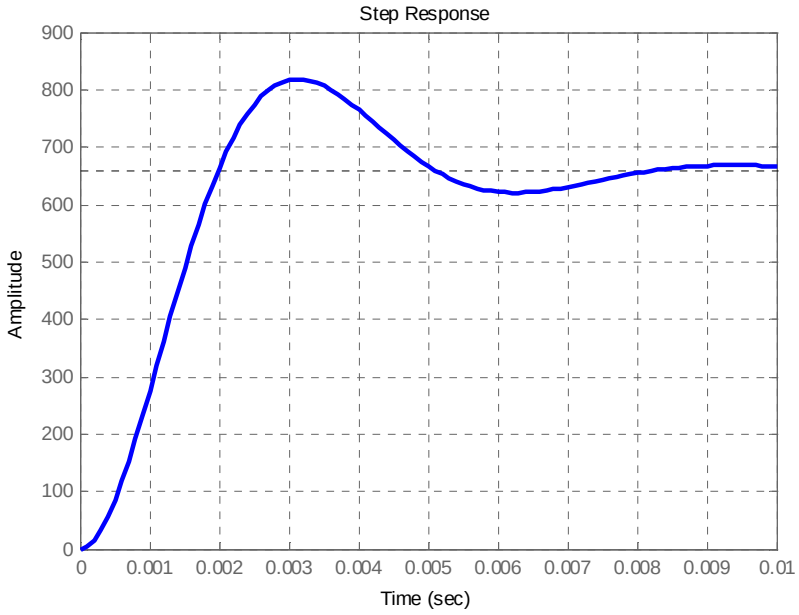

Figure 3.10: The unit step response of DC/DC resonant converter

Ziegler-Nichols second method is used for tuning PI controller. In this approach a proportional controller is developed as shown in Figure 3.11.

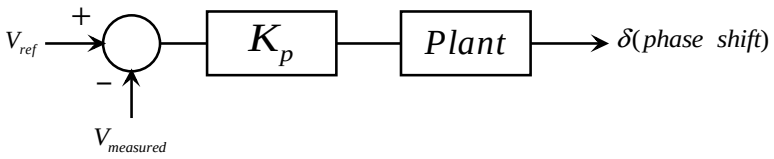

Figure 3.11: The proportional controller designed for Ziegler-Nichols second method

The proportional gain was increased until the unit step response of the system exhibits sustained oscillations for critical gain K_{cr} and with oscillation period of P_{cr}. Ogata [30] provides Ziegler-Nichols tuning rule for PI controller based on critical gain K_{cr} and critical period P_{cr} as follows,

$$K_p = 0.45K_{cr} = 0.005 \tag{3.13}$$

$$T_i = \frac{1}{1.2} P_{cr} = 1.2\,\text{sec} \tag{3.14}$$

$$G_C(s) = K_p \cdot \left(1 + \frac{1}{T_i s}\right) \tag{3.15}$$

Figure 3.13 compares the step response of the designed system in Figure 3.1 with the closed loop control system shown in Figure 3.12.

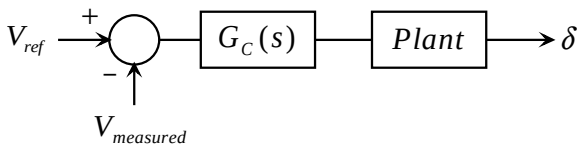

Figure 3.12: Closed loop control system of designed system

The step response of the mathematical and the actual system modeled in PSCAD/EMTDC show close results as depicted in Figure 3.13(a) and 3.13(b), where Figure 3.13(a) is the step response of the mathematical model and Figure 3.13(b) is the step response of the system modeled in PSCAD/EMTDC.

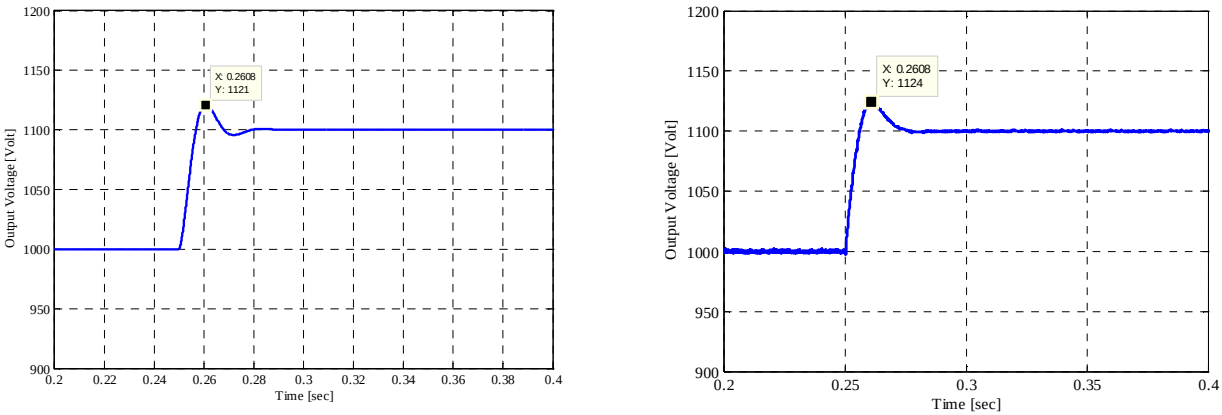

(a) (b)

Figure 3.13: Comparison the step response of the designed system in Figure 3.11 with the closed loop control system shown in Figure 3.12

3.3.3 Droop Control

To allow parallel operation of DC units, the voltage versus output current characteristic of each unit has a droop, it means a decrease in voltage should accompany an increase in output current as shown in Figure 3.14(a). The voltage droop of the DC unit is defined as the magnitude of the change in steady-state voltage, when the output of the unit is gradually reduced from one per-unit rated current to zero. Therefore, per-unit voltage droop is simply the magnitude of the slope as depicted in Figure 3.14(a) [1].

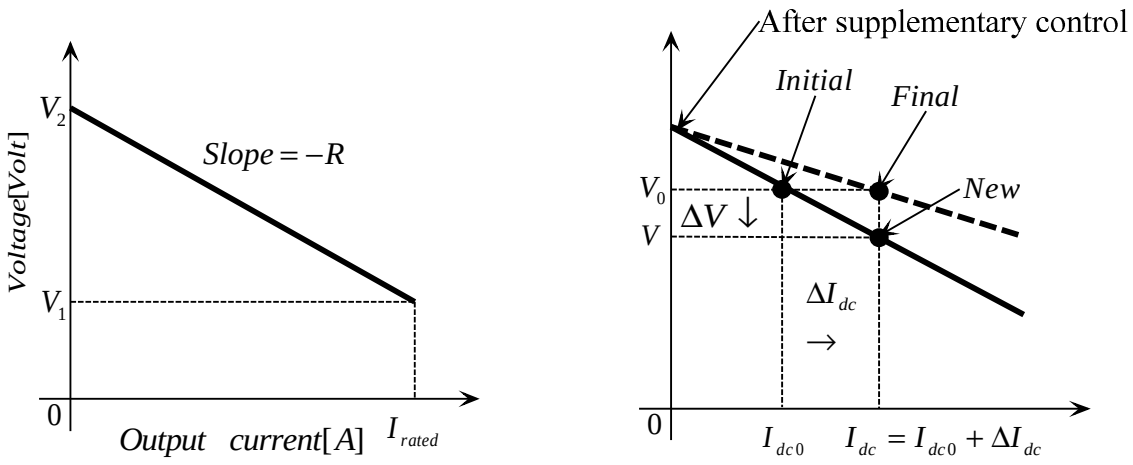

Figure 3.14: (a) Voltage versus output current characteristic, (b) before and after load increase and supplementary control [1]

The voltage droop from Figure 3.14(a) can be determined by,

$$R = \frac{V_2 - V_1}{I_{rated}} \tag{3.16}$$

where,

V_2 = No load voltage in Volt

V_1 = Voltage at rated current in Volt

I_{rated} = Rated current in Amp

Assume the DC unit is supplying output current I_{dc0} at V_0, when the load is increased to $I_{d0} + \Delta I_{dc}$, as shown in Figure 3.14(b), the voltage of the unit decreases. Therefore, more current is injected, and a new equilibrium occurs at a new voltage level $V_0 + \Delta V$. The unit will maintain its new operating point until the supplementary control increases the voltage to the desired value V_0 while providing the new output current I_{dc}.

3.4 EMT Simulation of Multiple DC/DC Resonant Converter under different Case Studies

This section investigates the overall performance of designed DC/DC resonant converter and the control system under two different case studies.

3.4.1 A Variable Load Connected to DC Bus

A DC plant consisting of ten DC/DC resonant converters each rated at 5kW are connected in parallel to maximize the injected current into the DC bus rated at 1000V. Figure 3.15 shows the described configuration. Each DC/DC resonant converter block is shown in Figure 3.1. Appendix B provides the detailed calculation and design of the DC/DC resonant converter.

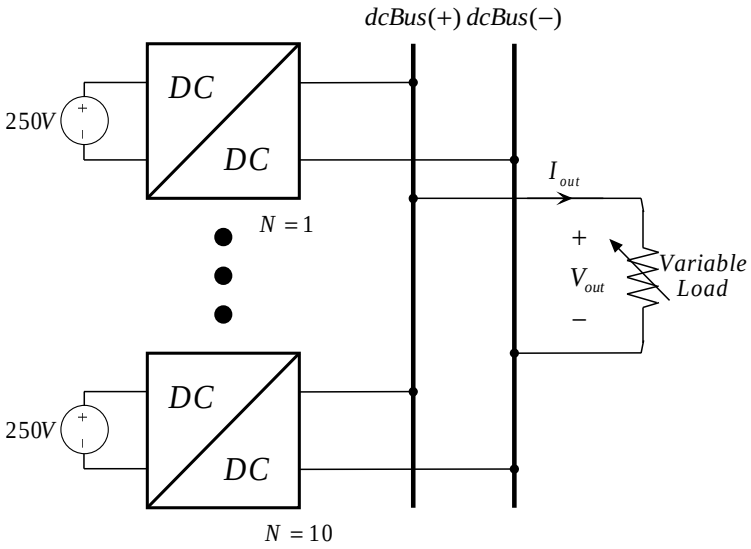

Figure 3.15: A DC plant connected to a variable load

Figure 3.16 depicts the output voltage across the load and its variable current. Note that the load change happens at a rate of 0.01 per second to mimic the load change in real application. The variable resistive load is modeled as a variable current source in PSCAD/EMTDC. At $t = 0.3\text{sec}$, the load current changes from 0.5A to 5A and remains constant until $t = 1.25\text{sec}$ where the load current reduces to 1A. The controller adjusted the phase such that the DC bus voltage remains constant at 1000V.

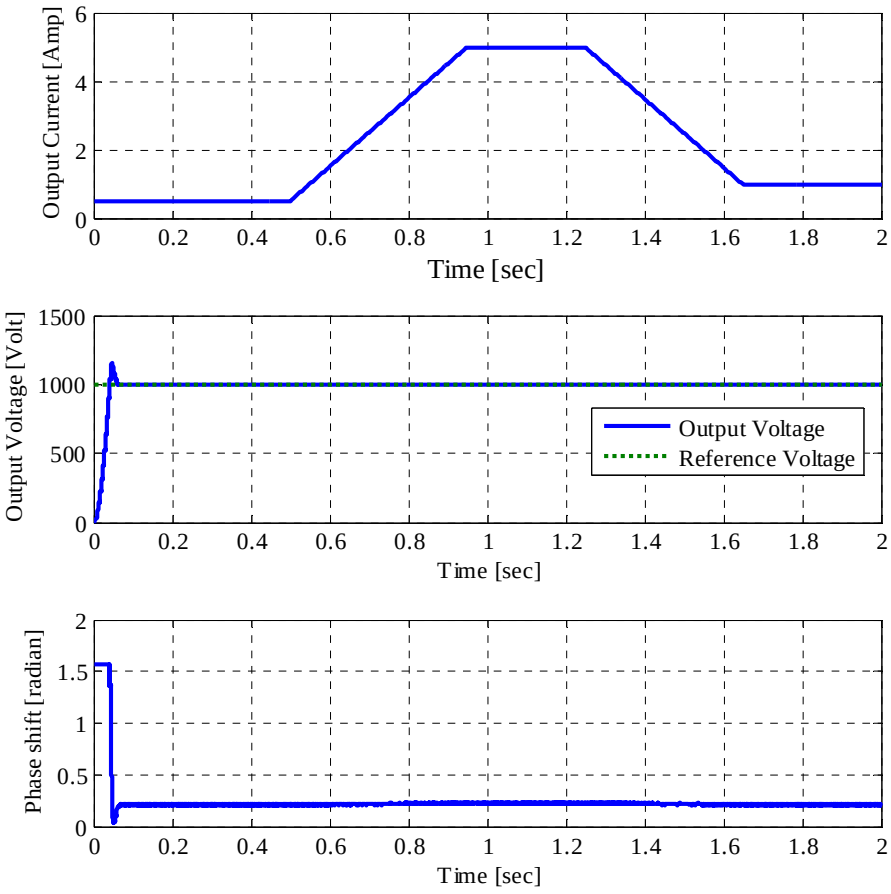

Figure 3.16: A DC bus voltage, current and phase shift

3.4.2 DC Plant Connected to the Grid through a Voltage-Source Converter

The designed DC plant cannot be connected to the grid directly. The voltage-source converter (VSC) technology needs to be implemented in order to convert the DC to an appropriate AC system. Figure 3.17 represents this configuration. VSC generates a 600V

three phase AC voltages, standard in Canada, where it steps up to 12.47kV line-to-line, 60Hz AC source through a y-y connected transformer.

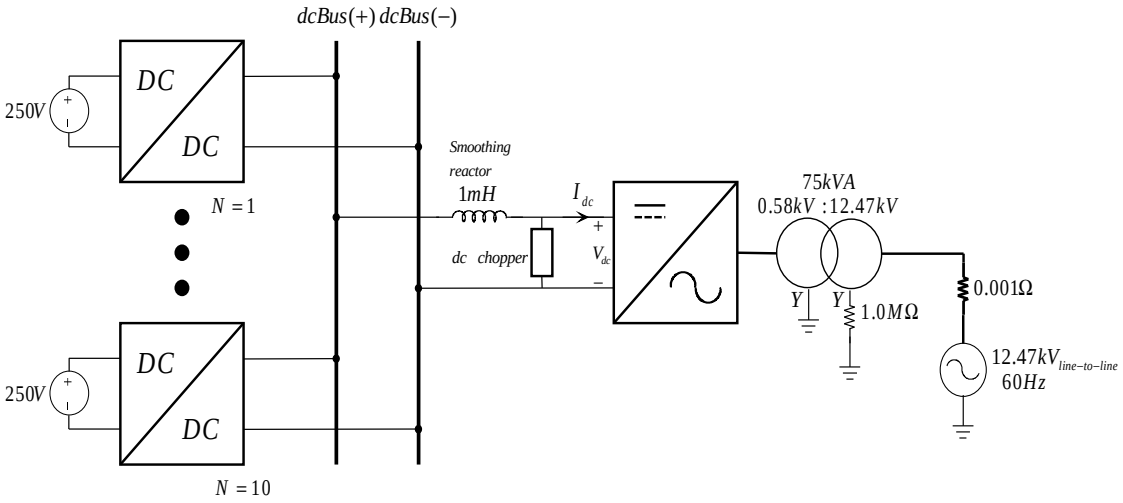

Figure 3.17: A DC plant connected to a 60Hz grid through a VSC

The power reference of VSC has changed from 50kW to – 50kW to demonstrate that the power can flow in both directions. The negative sign represents the direction of power from DC to AC. The reference power changes at 2.0sec at a rate of 0.1 per second as shown in Figure 3.18.

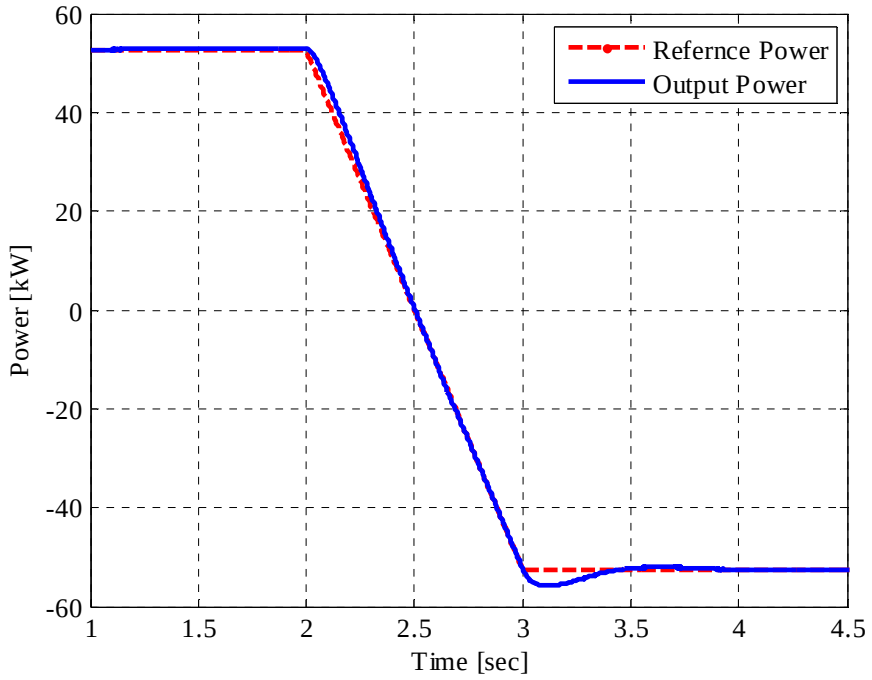

Figure 3.18: Power flow from AC to DC side

Figure 3.19 shows the total DC output current and DC bus voltage. Prior to $t = 2\,\text{sec}$, the current flowing to the DC sources while the DC bus voltage remains constant at 980V. This feature of DC/DC resonant converter allows replacing the voltage sources with energy storage elements where it can be charged whenever it is necessary. After $t = 3\,\text{sec}$, the DC side supplies power to the AC side while maintaining the DC bus voltage constant. Since the detailed model of VSC and DC/DC resonant converters were used, it required a long time to complete the simulation with the desired simulation time step. Chapter 4 will develop a mathematical model of the system based on generic state space averaging model, and will compare its results with the detailed model as well as the models developed in section 3.1.

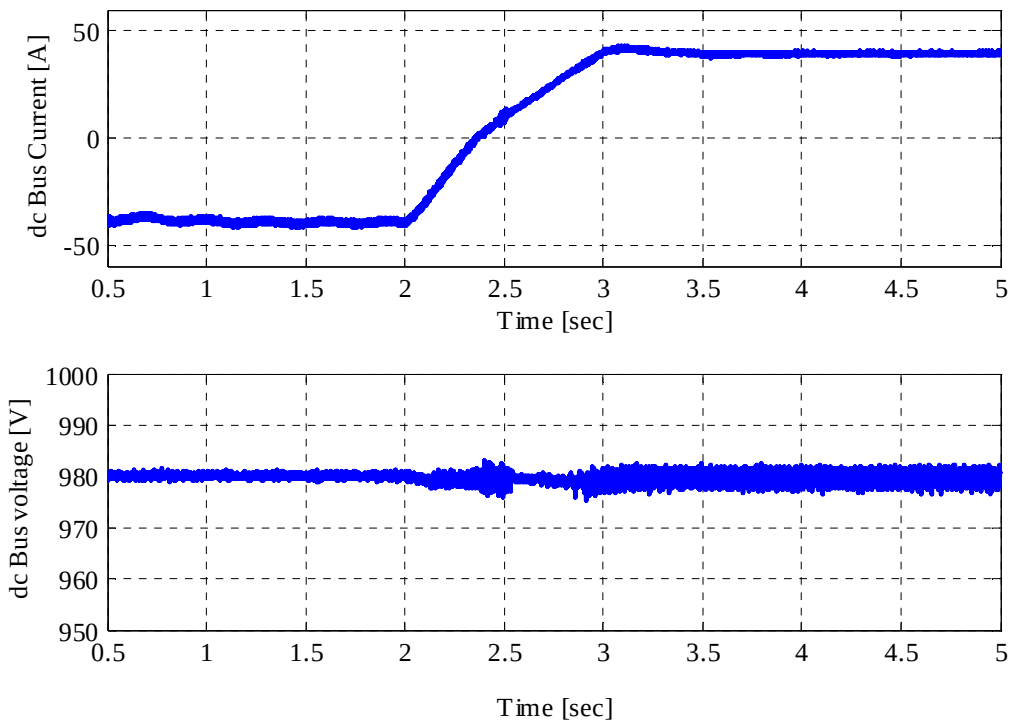

Figure 3.19: The total DC output current and DC bus voltage

Chapter 4

Generalized State Space Modeling of Resonant Converters

Power electronic switches are usually operated at high frequency. Therefore, it is necessary to use smaller simulation time steps, which can slow down the simulation to achieve more accurate results. The simulation run time can be more significant if the multiple converters with detailed power electronic components are used. In addition, a general pattern of the converter behavior is more important than its fine switching details in the development of power converter models. Therefore, this chapter introduces generalized state space modeling, its application to the DC/DC resonant converter, and finally demonstrates the time saving while comparing the average model results with detailed models.

4.1 Theory of Generalized State Space Averaging

The characteristic switching operation of power electronic converters leads to periodic changes in the circuit configuration and results in a non-linear dynamical system. For each combination of the states of the switching devices, a separate set of equations is to be defined to describe the circuit. Given that each switching state typically lasts for a short period of time and is followed by another state, the number of sets of equations describing the dynamics of the circuit becomes large and the successive solution requires massive and time-consuming calculation [35].

In generalized state space averaging technique, a single set of linear equations is defined by taking a linear average of the separate equations for each switching configuration of the circuit. Solution of power electronic circuits often reveals two components of response: a DC components and a varying component which is due to high frequency switching [35].

The generalize averaging method is developed based on the assumption that waveform $x(t)$ can be approximated on the interval $(t-T, t]$ with Fourier series representation of (4.1),

$$x(t-T+s) = \sum_{k=1,2,\ldots} \langle x(t) \rangle_k e^{jk\omega_s (t-T+s)} \tag{4.1}$$

where $\omega_s = \frac{2\pi}{T}$, $s \in (0, T]$, and $\langle x(t) \rangle_k$ are complex Fourier coefficients respectively [31]. The complex Fourier coefficients can also be determined as shown in (4.2).

$$\langle x \rangle_k = \frac{1}{T} \int_0^T x(t-T+s) \cdot e^{-jk\omega_s (t-T+s)} ds \tag{4.2}$$

Certain properties of Fourier coefficient such as differentiation with respect to time (4.3) and convolution (4.4) are necessary to be considered to analyze and convert state equations into complex form [31].

$$\frac{d}{dt}\langle x(t)\rangle_k = \left\langle \frac{d}{dt}x(t)\right\rangle_k - jk\omega_s\langle x(t)\rangle_k \tag{4.3}$$

$$\langle x\cdot y\rangle_k = \sum_i \langle x\rangle_{k-i}\cdot\langle y\rangle_i \tag{4.4}$$

Index zero indicates the DC component of a given waveform while index one specifies the fundamental component. The next section demonstrates the application of averaging model to the resonant converters.

4.2 Application to Resonant Converters

Since the resonant converters are usually operating at high switching frequency, a small simulation time step is needed in order to achieve accurate results. Sanders [31] introduced a much broader approach of state-space averaging which is more effective and applicable to variety of circuits. This section provides detail mathematical modeling of resonant converter as well as dynamic modeling of VSC.

4.2.1 Resonant Converter Average Model

The circuit presented in Figure 3.1 was used as a reference to develop the KVL and KCL equations. As explained earlier in Chapter 2, the output voltage of the inverter looks like a square wave function with the frequency equals to the switching frequency. Therefore, the voltage waveform can be shown mathematically as follow,

$$V_d = V_{dc}\cdot sign(\sin\omega_s t) \tag{4.5}$$

where V_{dc} is the magnitude of input voltage source and $sign(x)$ function is defined as (4.6).

$$sign(x) = \begin{cases} 1 & x > 0 \\ 0 & x = 0 \\ -1 & x < 0 \end{cases} \tag{4.6}$$

As discussed in section 3.1.2, the input voltage to the rectifier is in phase with the resonant tank inductor current and can be shown as follows,

$$v_{rectifier} = v_{out} \cdot sign(i_{Lr}) \tag{4.7}$$

Similarly, the rectifier output current can be mathematically shown as,

$$i_{rectifier} = abs(i_{Lr}) \tag{4.8}$$

Equation (4.9) to (4.12) summarizes the mathematical representation of system equations.

$$\frac{di_{Lr}}{dt} = \frac{1}{L_r}\left(V_d - R_r i_{Lr} - v_{Cr} - \frac{1}{n} v_{out} \cdot sign(i_{Lr})\right) \tag{4.9}$$

$$\frac{dv_{Cr}}{dt} = \frac{1}{C_r} i_{Lr} \tag{4.10}$$

$$\frac{dv_{out}}{dt} = \frac{1}{C_f}\left(\frac{1}{n} abs(i_{Lr}) - \frac{v_{out}}{R_{load}}\right) \tag{4.11}$$

$$V_d = V_{dc} \cdot sign(\sin \omega_s t) \tag{4.12}$$

As shown in Chapter 3, some states of DC/DC resonant converter display purely sinusoidal waveform, which contains only fundamental frequency, or pure DC components. Therefore, only index zero and one are considered in order to determine a generic state space average model. Appendix F provides the detailed mathematical calculations.

4.2.2 VSC Average Model

Peralta [32] proposed a dynamic average model where IGBTs are not modeled and behavior of VSC is presented by controlled voltage and current sources. The magnitude of voltage sources are controlled by VSC vector control systems. Assuming a lossless converter and from conservation of energy the power on the AC side has to be equal to the power on the DC side as shown in (4.13). Moreover, the DC current can be determined by (4.14) and injected as a current source to the DC side.

$$P_{ac} = P_{dc} \tag{4.13}$$

$$v_a \cdot i_a + v_b \cdot i_b + v_c \cdot i_c = V_{dc} \cdot I_{dc} \tag{4.14}$$

Figure 4.1 shows the controlled voltage and current source representation of VSC.

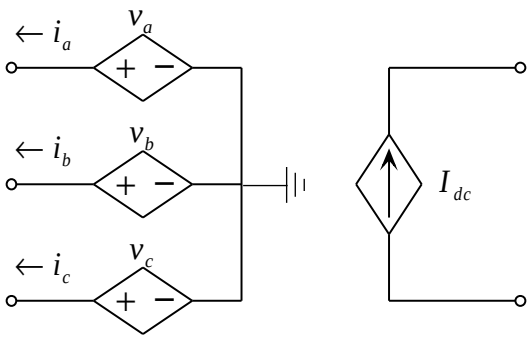

Figure 4.1: The controlled voltage and current source representation of VSC

4.3 Simulation of the System and Demonstration of Time Saving

Two different cases are developed to demonstrate the accuracy and time saving of average modeling.

a. This case modeled the DC/DC resonant converter as discussed in Chapter 3 presented in Figure 3.4, and VSC with the controlled voltage and current source as shown in Figure 4.1 and 4.2.
b. This case modeled the DC/DC resonant converter with the generalized state space model developed in section 4.2.1, and VSC with the controlled voltage and current source as shown in Figure 4.1 and 4.2.

The circuit presented in Figure 3.17 was considered for the average model study. The simulation was run for 4 seconds. Table 4.1 tabulates the summary of operating system used for the study.

Table 4.1: Operating system specification

Windows edition	Windows 7 Professional
Processor	Intel(R) Core(TM) i7-2640M CPU at 2.80 GHz
Installed memory (RAM)	8.00 GB
System type	64-bit operating system

Table 4.2 compares the total simulation runtime of all three approaches. The simulation runtime reduced drastically by using generalized state space and dynamic averaging model. Since the simulation runtime of generalized state space averaging model and dynamic averaging model is fairly close, either one approach can be used to simplify the complex models. However, the complexity of system will result in more complex system of equations and will be time consuming and more difficult to generate the mathematical model for such a system. Therefore, a dynamic averaging model is simpler in terms of development and can be considered for more complex systems. In addition, the generalized state space averaging model shows a dependency on the

simulation time step. Increasing the simulation time step can result in numerical inaccuracy for this approach. Therefore, the simulation time step cannot be increased to a very large number.

Table 4.2: The simulation runtime comparison

	Runtime [hr:min:sec]	Simulation time step
Detailed model	01:02:43	$2\mu s$
Dynamic averaging model	00:02:48	$50\ \mu s$
Generalized state space model	00:01:22	$50\ \mu s$

Figure 4.2 compares the results of all three approaches at steady state. The AC current and voltage waveforms in high voltage side of the VSC are presented in Figure 4.2 (a) and (b) respectively. The generalized state space and dynamic averaging model results are very close to the detailed model.

The DC bus voltage and current are shown in Figure 4.2 (c) and (d) respectively. Ignoring the varying component of the stated waveforms which is due to high frequency switching of power electronic devices, the dynamic and generalized state space averaging model of are demonstrated a very close results. The small difference is due to ignoring the resistivity of IGBT and diode switches in dynamic averaging and generalized state space models.

The reference voltage is generated by VSC control system in order to control the operation of switches. The results of dynamic averaging model and generalized state space model are close to the detailed model results if the high frequency component of switching devices has been ignored.

Chapter 5 presents the functionality and the verification of designed DC/DC resonant converter.

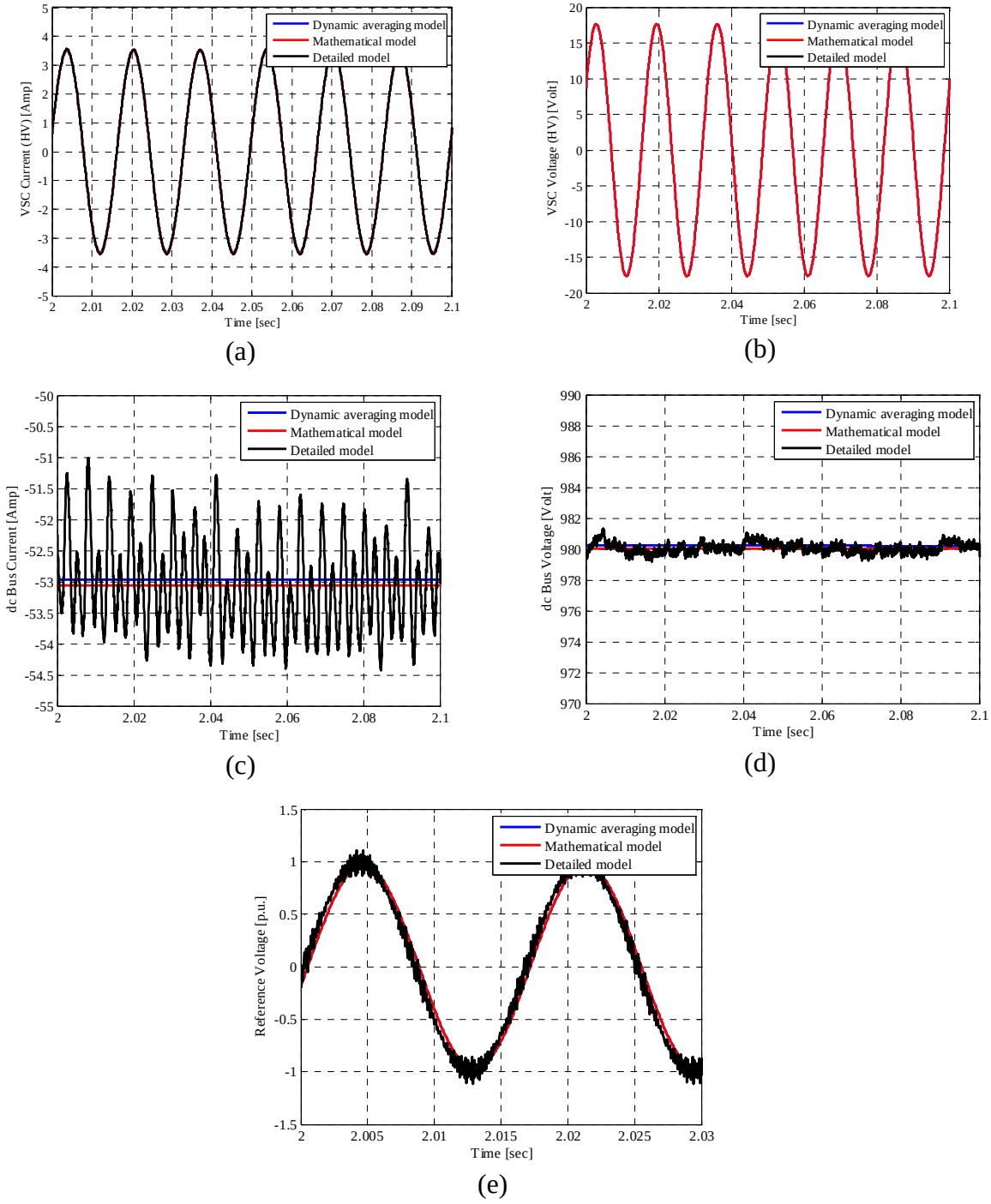

Figure 4.2: Results comparison among dynamic averaging model, mathematical (generalized state space) model, and detail model

Chapter 5

Design Verification and Testing

Two small scale DC/DC resonant converters are designed and implemented as shown in Figure 5.1. Appendix A contains design specifications and calculations of a 100W, 50V DC/DC resonant converters.

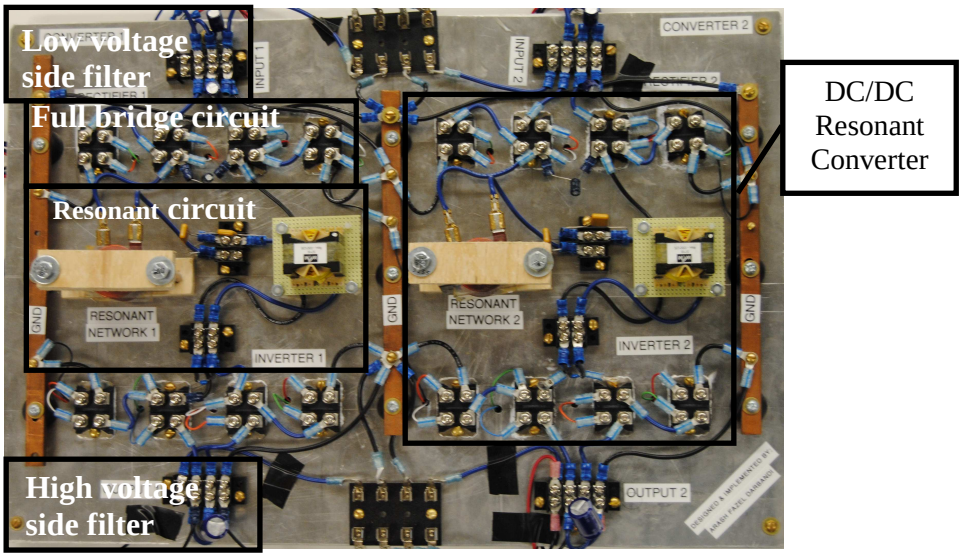

Figure 5.1: Two 100W, 50V DC/DC resonant converters in parallel

Multiple tests were performed to verify the designed DC/DC resonant converters. This chapter presents the verification test results and compares with theoretical and simulation results.

5.1 Demonstrate Bidirectional Operation of DC/DC Resonant Converter

As discussed in Chapter 2 and 3, the DC/DC resonant converter is capable of controlling power flow in both directions. The power flow direction can be controlled by adjusting the phase shift of the full-bridge rectifier. A fixed 25Ω resistive load is connected to the dc bus. A 25V power supply is connected to the input of each DC/DC resonant converter. Two DC/DC resonant converters are connected in parallel to share the load current and maintain the DC bus voltage at 50V. Figure 5.2 shows the circuit under verification.

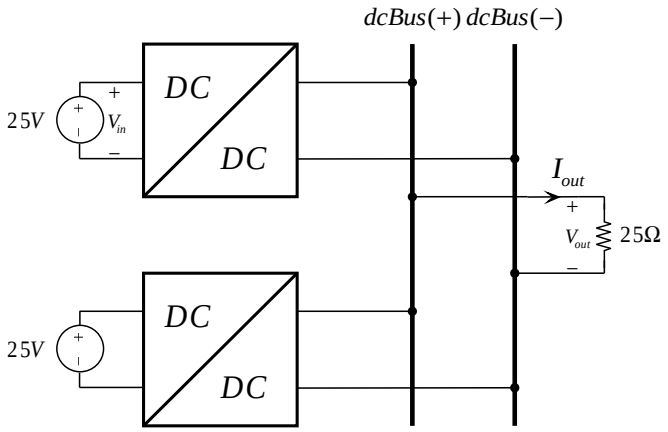

Figure 5.2: Two DC/DC resonant converters in parallel are feeding a resistive load

Figure 5.3 and 5.4 show the dc bus voltage and the output current of each DC/DC resonant converter respectively. The DC bus voltage remains constant at 50V while each converter shares the load current. Since the power supplies are identical, the load current has been shared equally between the power supplies.

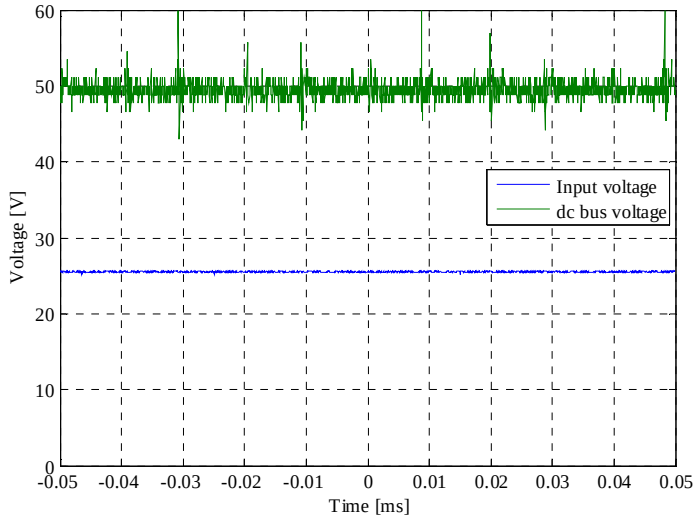

Figure 5.3: Input and DC bus voltage

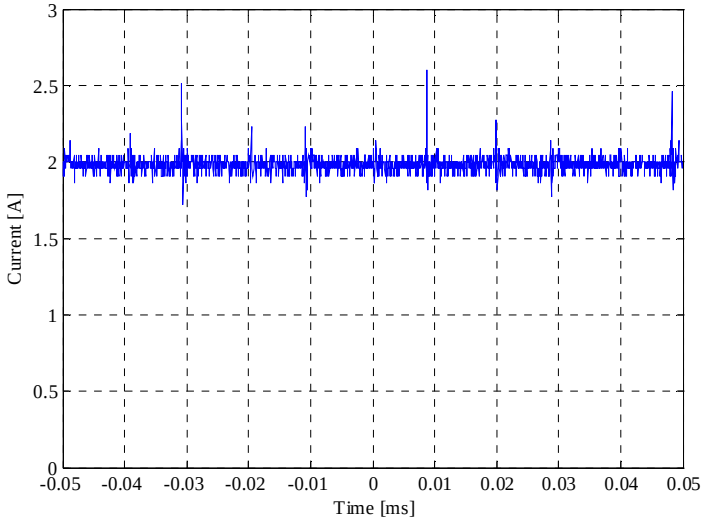

Figure 5.4: The output current of each DC/DC resonant converter

Figure 5.5 and 5.6 show the resonant circuit current measured across the series capacitor and the full-bridge inverter output voltage. As shown in section 2.4, the resonant circuit is a good quality sinusoidal while the full-bridge inverter output voltage is a square wave. The efficiency of the system shown in Figure 5.2 is measured and calculated as shown in (5.1). The designed DC/DC resonant converter demonstrates the much higher efficiency than available DC/DC converters with an efficiency of 80-88% [27].

$$\eta = \frac{P_{out}}{P_{in}} = \frac{49.56 \times 1.98}{2 \times 25.4 \times 2.01} = 96\% \tag{5.1}$$

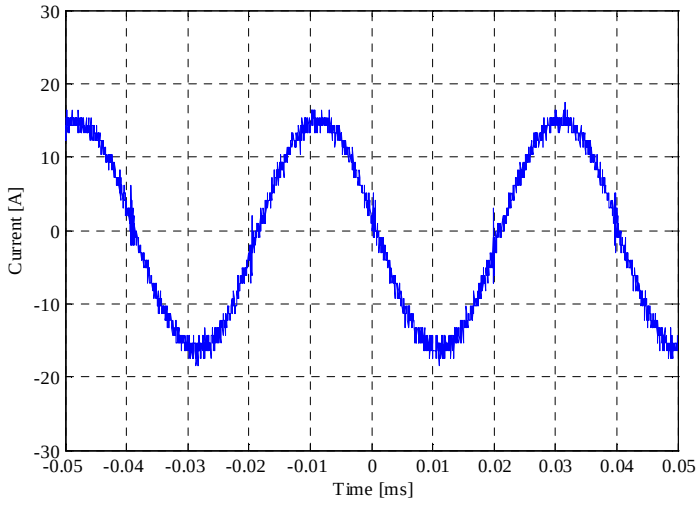

Figure 5.5: Resonant circuit current (i_{Lr})

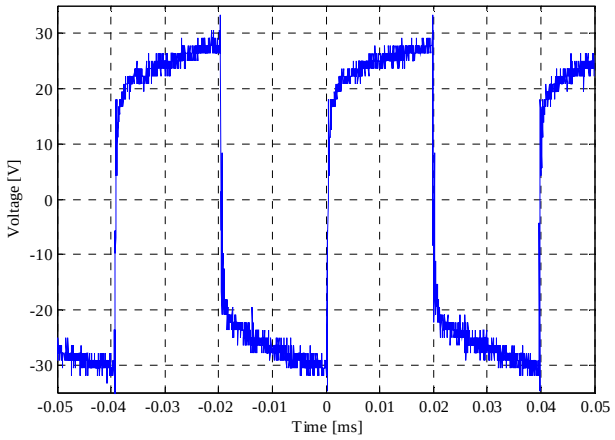

Figure 5.6: The full-bridge output voltage at 25.3kHz

The circuit shown in Figure 5.2 was modified to demonstrate the direction of power flow from DC bus to the resistive load as shown in Figure 5.7.

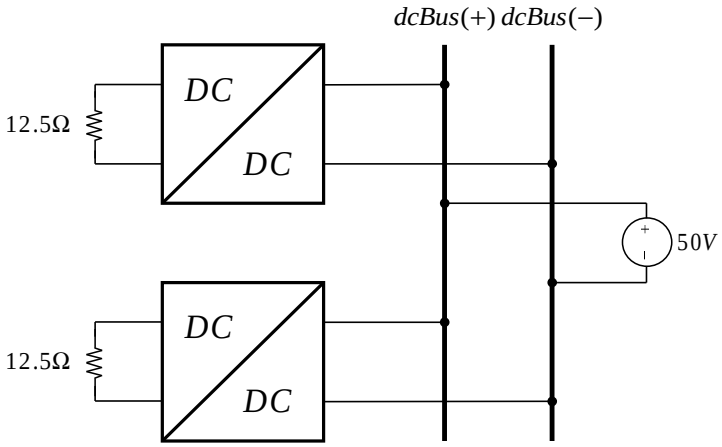

Figure 5.7: The power flows from the dc bus to the resistive loads

Figure 5.8 and 5.9 show the load voltage and the input current of each DC/DC resonant converter respectively. The voltage across each load remains constant at 25V.

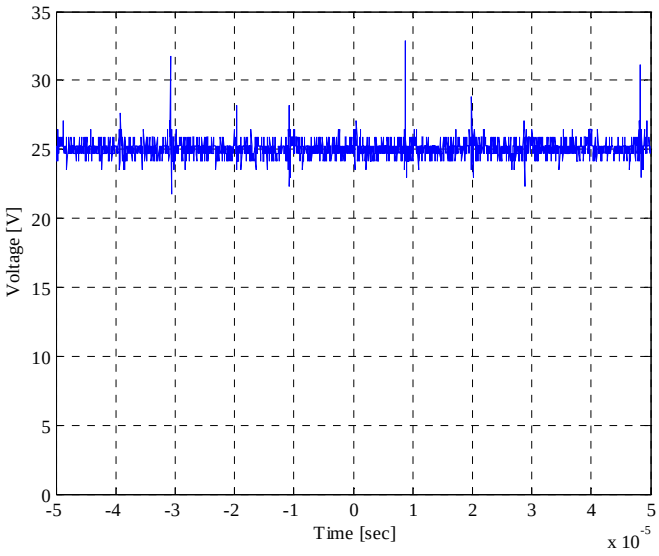

Figure 5.8: Load voltage

5.2 Demonstrate Functionality of DC/DC Resonant Converters with VSC and AC system

Real-Time Digital Simulator (RTDS) is a real-time power system simulation tool. It consists of custom software running on a PC and dedicated hardware that calculates and generates the real-time signals. RTDS can be interfaced with the external electrical equipment to simulate and test the functionality of each electrical system.

In this test, an AC motor is running on a three-phase balanced AC voltage. An AC motor drive is developed using a pulse-width modulation (PWM) technique by feeding a DC bus into a VSC located in LabVolt system, which is a small scale unit of actual equipment such as motors, power electronic system and loads. The PWM control signals were implemented in RTDS. The DC/DC resonant converter is responsible to maintain

the DC bus voltage at a fixed value throughout the operation of AC motor. Figure 5.9 shows the circuit under consideration.

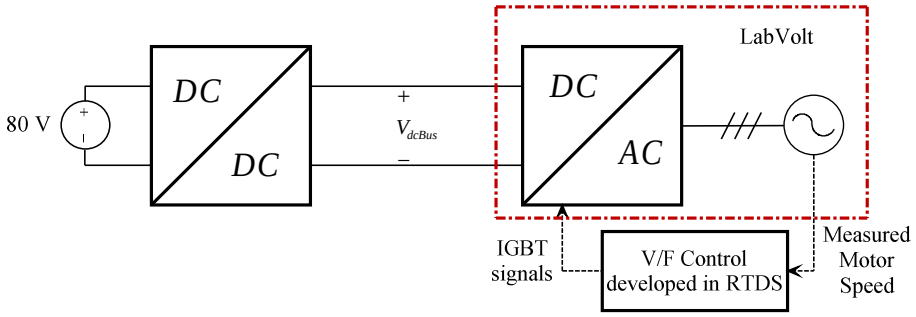

Figure 5.9: A DC/DC resonant converter is feeding an AC motor through a VSC

The motor speed changes from 500rpm to 700rpm to 400rpm to validate the performance of the DC/DC resonant converter and the motor drive control system. Figures 5.10 and 5.11 depict the DC bus voltage and the stator current throughout its operation. The voltage remains at 160V even though the motor speed changes.

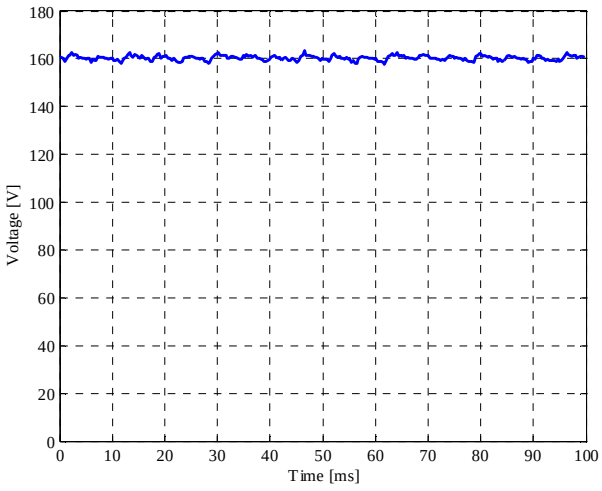

Figure 5.10: The DC bus voltage

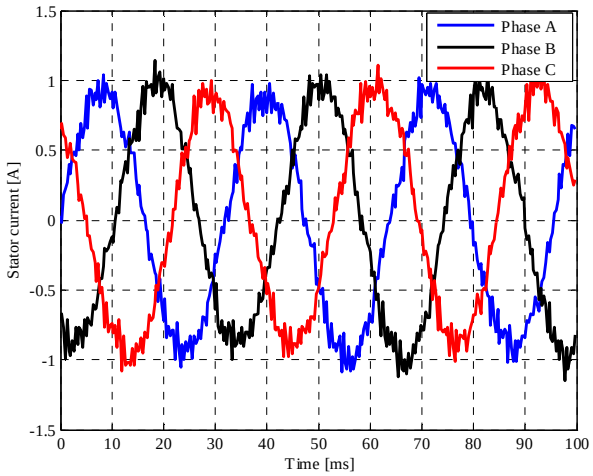

Figure 5.11: The three phase stator current

Figure 5.12 and 5.13 show the change in motor speed and the voltage-frequency control response during the speed change.

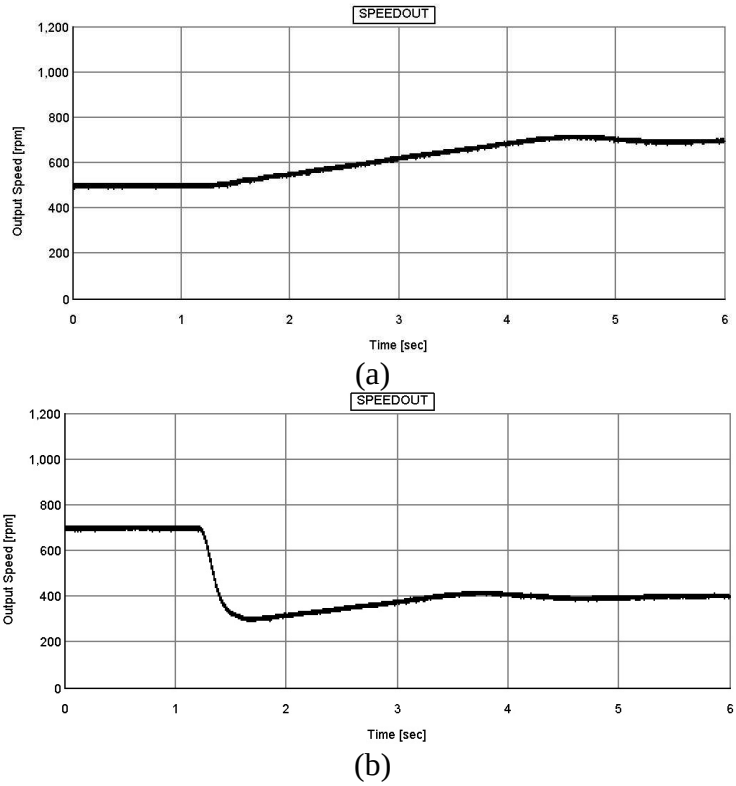

Figure 5.12: (a) The motor speed change from 500rpm to 700rpm (b) the motor speed changes from 700rpm to 400rpm

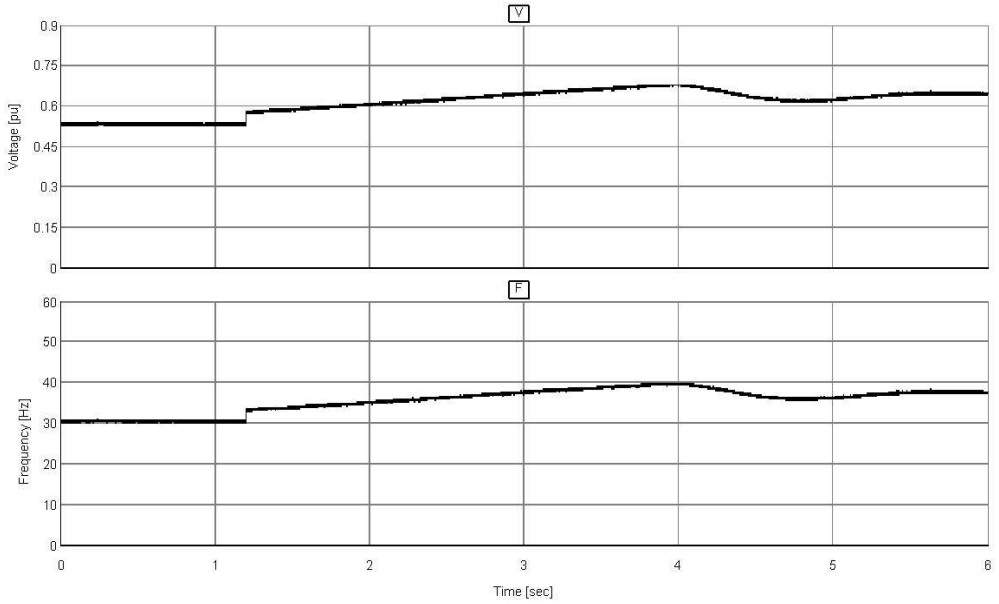

(a)

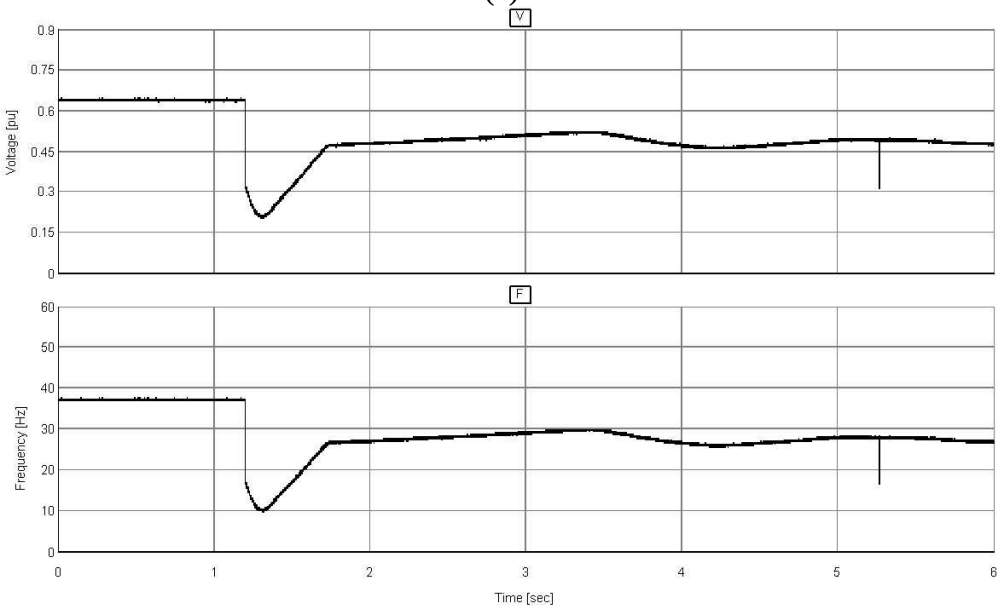

(b)

Figure 5.13: (a) The V/f control response when motor speed change from 500rpm to 700rpm (b) the V/f control response when motor speed changes from 700rpm to 400rpm

This experiment demonstrates the functionality and compatibility of a DC/DC resonant converter with AC system through a VSC.

Chapter 6

Conclusions, Contributions and Recommendations

6.1 Conclusions and Contributions

The main objective of this research was to investigate the applicability of DC/DC resonant converter in power system. This thesis investigated the functionality and feasibility of resonant DC/DC conversion in the power system applications. In particular the following items are observed:

- A series of literature surveys were performed to collect information in regards to DC/DC resonant converter. It was found that DC/DC resonant converters had less switching losses due to operating under soft-switching techniques, and required simpler control system.
- The design and PSCAD/EMTDC simulation took into account the special requirements of a 600V AC grid connection. It was observed that the DC/DC resonant converters are capable of transferring power in both directions, and

demonstrated less losses compared to typical PWM based DC/DC converters. DC/DC resonant converter also demonstrated controllability over various ranges of resistive load. Therefore, it showed more stability during load change when connected to the grid.

- The thesis also developed two different circuit averaging techniques, dynamic averaging model and generalized state space averaging model, to verify the computational efficiency of the new techniques for a complex system. The average models were validated by comparing their response to the original circuit. It was observed that the generalized state space averaging model shows dependency on the simulation time step to solve the defined system differential equations. Increasing the simulation time step can result in numerical inaccuracy for this approach. Therefore, the simulation time step cannot be increased to a very large number. The dynamic averaging model was determined to be sufficient enough for simplifying the larger systems.
- Two DC/DC resonant converters were constructed and tested. It was observed during the experiments that DC/DC resonant converters could operate in both directions and was capable of interfacing with VSC and AC system.

6.2 Recommendations for Future Work

The DC/DC resonant converter has proven that it is capable of performing in the power system industries. However, further research into the system will be valuable. For example, implementation and verification of a full scale DC/DC resonant converter can provide the opportunity for replacing existing DC/DC converters with this new

development. In addition, the interaction of DC/DC resonant converter with existing DC grid system and its performance during the DC or AC fault can provide in-depth analysis of this new development.

Bibliography

[1] J.J. Grainger and W.D. Stevenson Jr., *Power System Analysis,* McGraw-Hill, 1994.

[2] M.H. Rashid, *Power Electronics,* 3rd Ed. Upper Saddle River, NJ: Prentice Hall, 2004.

[3] M.K. Kazimierczuk and D. Czarkowski, *Resonant Power Converters,* Hoboken, NJ: John Wiley & Sons, 2011.

[4] R.W. Erickson and D. Maksimović, *Fundamental of Power Electronics,* 2nd Ed. Norwall, MA: Kluwer Acdemic, 2001.

[5] Y. Zhang and P.C. Sen, "D-Q models for resonant converters," in *Power Electronics Specialists Conference,* Aachen, Germany, 2004, vol. 3, pp. 1749-1753.

[6] S. Golestan, M. Joorabian, H. Rastegar, A. Roshan and J.M. Guerrero, "Droop based control of parallel-connected single-phase inverters in D-Q rotating frame," in *Industrial Technology,* Churchill, Australia, 2009, pp. 1-6.

[7] L. Gyugyi and F. Cibulka, "The high-frequency base converter – A new approach to static high-power conversion," *IEEE Transaction on Industry Applications,* vol. IA-15, no. 4, pp. 420-429, 1979.

[8] X. Li and A.K.S. Bhat, "Analysis and design of high-frequency isolated dual-bridge series resonant dc/dc converter," *IEEE Transactions on Power Electronics,* vol. 25, no. 4, pp. 850-862, 2010.

[9] H. Krishnaswai and N. Mohan, “Three-port series-resonant dc-dc converter to interface renewable energy sources with bidirectional load and energy storage ports,” *IEEE Transactions on Power Electronics*, vol. 24, no. 10, pp. 2289-2297, 2009.

[10] S. Zheng and D. Czarkowski, “Dynamics of a phase-controlled series-parallel resonant converter,” in *Circuits and Systems*, Scottsdale, Arizona, 2002, vol. 3, 819-822.

[11] M.Z. Youssef and P.K. Jain, “A review and performance evaluation of control techniques in resonant converters,” in *IEEE Industrial Electronics Society*, Busan, Korea, 2004, pp. 215-221.

[12] H. Wang, J. Clare, P. Zanchetta, P. Wheeler, D. Cook and M. Bland, “State space ZCS control for three-phase resonant converter,” in *Industrial Electronics*, Orlando, Florida, 2008, pp. 977-982.

[13] S. Zheng and D. Czarkowski, “Modeling and digital control of a phase-controlled series-parallel resonant converter,” *IEEE Transactions on Industrial Electronics*, vol. 54, no. 2, pp. 707-715, 2007.

[14] O. Ojo, “Robust control of series parallel resonant converters,” *IEEE Control Theory and Applications*, vol. 142, no. 5, pp. 401-410, 1995.

[15] A.F. Witulski and R.W. Erickson, “Steady-state analysis of the series resonant converter,” *IEEE Transaction on Aerospace and Electronic Systems*, vol. AES-21, no. 6, pp. 791-799, 1985.

[16] West Coast Magnetics. *Switchmode power supply transformer design*. West Coat Magnetics, Stockton, CA. Available: http://www.wcmagnetics.com/images/pdf/appnote11.28.10.pdf [June 12, 2011].

[17] R.W. Erickson and D. Maksimović, *Fundamental of Power Electronics*, 2nd Ed. Norwall, MA: Kluwer Acdemic, 2001.

[18] B. Mammano. *Resonant mode converter topologies*. Texas Instruments, Dallas, Texas. Available: http://www.ti.com/lit/ml/slup085/slup085.pdf [April 10, 2011].

[19] H. Choi, "Design consideration of half-bridge LLC resonant converter," *Journal of power electronics*, vol. 7, no. 1, pp. 13-20, 2007.

[20] F. Krismer, J. Biela and J.W. Kolar, "A comparative evaluation of isolated bi-directional dc/dc converters with wide input and output voltage range," in *Industry Application Conference*, Kowloon, Hong Kong, 2005, vol. 1, pp. 599-606.

[21] R.P. Severns and G. Bloom, *Modern DC-to-DC Switchmode Power Converter Circuits*, New York: Van Nostrand Reinhold, 1985.

[22] R.G. Hoft, *Semiconductor Power Electronics*, New York: Van Nostrand Reinhold, 1986.

[23] J.G. Kassakian, M.S. Schlecht, and G.C. Verghese, *Principles of Power Electronics*, Reading, MA: Addison-Welsley, 1991.

[24] N. Mohan, T.M. Undeland, and W.P. Robbins, *Power Electronics: Converters, Applications and Design*, 3rd Ed. Hoboken, NJ: John Wiley & Sons, 2003.

[25] I. Batarseh, *Power Electronic Circuits*, Hoboken, NJ: John Wiley & Sons, 2004.

[26] M.K. Kazimierczuk, *Electronic Devices, A Design Approach*, Upper Saddle River, NJ: Prentice Hall, 2004.

[27] M.K. Kazimierczuk, *Pulse-Width Modulated DC-DC Power Converters*, Chichester, UK: John Wiley & Sons, 2008.

[28] M.K. Kazimierczuk, *High-Frequency Magnetic Components*, Chichester, UK: John Wiley & Sons, 2008.

[29] "Electric filter design," class notes for ECE4200, Department of Electrical and Computer Engineering, University of Manitoba, 2010.

[30] K. Ogata, *Modern Control Engineering*, 4th Ed. Prentice Hall, 2002.

[31] S.R. Sanders, J.M. Noworolski, X.Z. Liu and G.C. Verghese, "Generalized averaging method for power conversion circuits," *IEEE Transactions on Power Electronics*, vol. 6, no. 2, pp. 251-259, 1991.

[32] J. Peralta, H. Saad, S. Dennetière, J. Mahseredjian and S. Nguefeu, "Detailed and averaged models for a 401-level MC-HVDC system," *IEEE Transactions on Power Delivery*, vol. 27, no. 3, pp. 1501-1508, 2012.

[33] IXYS Corporation, "*HiPerFAST™ IGBTs with Diode.*" Milpitas, CA: IXYS corporation, 2009.

[34] D. Trim, *Calculus for Engineers*, 3rd Ed. Prentice Hall, 2004.

[35] L.S.K. Kothalawalage, "Computationally efficient simulation-based sensitivity analysis method for power electronic circuits," M.Sc. thesis, Department of Electrical and Computer Engineering, University of Manitoba, Winnipeg, MB, 2010.

Appendix A

Design of 100 W, 50 V DC/DC Resonant Converter

This chapter contains design specifications and calculations of a 100 W, 50V DC/DC resonant converter. Formulas used in this chapter are originally developed in [3].

Design specifications, $V_I = 25V$, $V_O = 50V$, $I_O = 0-2A$

The maximum output power is,

$$P_{O\max} = V_O I_{O\max} = 50 \times 2 = 100W \qquad \text{(A.1)}$$

The full load resistance of the converter is,

$$R_{L\min} = \frac{V_O}{I_{O\max}} = \frac{50}{2} = 25\Omega \qquad \text{(A.2)}$$

Assuming that the total efficiency of the converter is $\eta = 90\%$, the maximum DC input power can be calculated as,

$$P_{\mathrm{Im}ax} = \frac{P_{O\max}}{0.9} = \frac{100}{0.9} = 111.11W \qquad \text{(A.3)}$$

And the maximum value of the DC input current can also be calculated as,

$$I_{\mathrm{Im}ax} = \frac{P_{\mathrm{Im}ax}}{V_I} = \frac{111.11}{25} = 4.44A \tag{A.4}$$

The equivalent input resistance of the rectifier at full load can be determined as,

($n = 0.5, \eta_{tr} = 0.98, r_{DS} = r_{LF} = 0.02\Omega, Q_g = 146\ nC, V_{GSpp} = 15V, f = 25300\ Hz$) [33].

$$R_{i\min} = \frac{\pi^2 n^2 R_{L\min}}{8\eta_{tr}} \left(1 + \frac{r_{DS} + r_{LF}}{R_{L\min}} + \frac{2fQ_g V_{GSpp}}{P_{O\max}} \right) = \tag{A.5}$$

$$= \frac{\pi^2 0.5^2 25}{8 \times 0.98} \left(1 + \frac{0.02 + 0.02}{25} + \frac{2 \times 25300 \times 146 \times 10^{-9} \times 15}{100} \right) = 7.87\Omega$$

The efficiency of the rectifier η_R,

$$\eta_R = \frac{\eta_{tr}}{1 + \frac{r_{DS} + r_{LF}}{R_{L\min}} + \frac{2fQ_g V_{GSpp}}{P_{O\max}}} \tag{A.6}$$

$$= \frac{0.98}{1 + \frac{0.02 + 0.02}{25} + \frac{2 \times 25300 \times 146 \times 10^{-9} \times 15}{100}} = 0.977$$

The voltage transfer function of the rectifier can be found as follow,

$$\left| M_{VR} \right| = \frac{2\sqrt{2}\eta_{tr}}{\pi n \cdot \left(1 + \frac{r_{DS} + r_{LF}}{R_{L\min}} + \frac{2fQ_g V_{GSpp}}{P_{O\max}} \right)} \tag{A.7}$$

$$= \frac{2\sqrt{2} \times 0.98}{0.5\pi \left(1 + \frac{0.02 + 0.02}{25} + \frac{2 \times 25300 \times 146 \times 10^{-9} \times 15}{100} \right)} = 1.76$$

The voltage transfer function of the converter,

$$M_V = \frac{V_O}{V_I} = \frac{50}{25} = 2 \tag{A.8}$$

Assume $n = 0.5, \eta_{tr} = 0.98, \eta_I = 0.97$, $A = 1, Q_L = 2$ and $f_0 = 32.22\,kHz$, by solving (A.9) the normalized switching frequency can be calculated as $\frac{f}{f_0} = 0.7852$ and $f = 25.3kHz$.

$$M_V = \frac{8\eta_I \eta_{tr}}{n\pi^2 \sqrt{(1+A)^2\left[1-\left(\frac{f}{f_0}\right)^2\right]^2 + \left[\frac{1}{Q_L}\left(\frac{f}{f_0} - \frac{f_0}{f}\frac{A}{1+A}\right)\right]^2}} \tag{A.9}$$

The component values of the resonant circuit can be determined as follow,

$$L = \frac{R_{i\min}}{\omega_0 Q_L} = \frac{7.87}{2\pi \times 32220 \times 2} = 19.44\mu H \rightarrow 20\mu H \tag{A.10}$$

$$C = \frac{Q_L}{\omega_0 R_{i\min}} = \frac{2}{2\pi \times 32220 \times 7.87} = 1.26\mu F \tag{A.11}$$

$$C_1 = C \cdot \left(1 + \frac{1}{A}\right) = 2C = 2.51\mu F \rightarrow 2.7\mu F \tag{A.12}$$

$$C_2 = C \cdot (1+A) = 2C = 2.51\mu F \xrightarrow{on\,Transfomer\,Secondary} 0.68\mu F \tag{A.13}$$

Appendix B

Design of 5kW, 1000V DC/DC Resonant Converter

This chapter contains design specifications and calculations of a 5 kW, 1000 V DC/DC resonant converter. Formulas used in this chapter are originally developed in [3].

Design specifications, $V_I = 250\ V$, $V_O = 1000\,V$, $I_O = 0-5A$

The maximum output power is,

$$P_{O\max} = V_O I_{O\max} = 1000 \times 5 = 5kW \tag{B.1}$$

The full load resistance of the converter is,

$$R_{L\min} = \frac{V_O}{I_{O\max}} = \frac{1000}{5} = 200\Omega \tag{B.2}$$

Assuming that the total efficiency of the converter is $\eta = 90\%$, the maximum DC input power can be calculated as,

$$P_{\mathrm{Im}ax} = \frac{P_{O\max}}{0.9} = \frac{5000}{0.9} = 5.56kW \tag{B.3}$$

And the maximum value of the DC input current can also be calculated as,

$$I_{\mathrm{Im}ax} = \frac{P_{\mathrm{Im}ax}}{V_I} = \frac{5560}{250} = 22.2A \tag{B.4}$$

The equivalent input resistance of the rectifier at full load can be determined as,

($n = 0.25, \eta_{tr} = 0.98, r_{DS} = r_{LF} = 0.02\Omega, Q_g = 146nC, V_{GSpp} = 15V$, $f = 25300\ \ Hz$) [33]

$$R_{i\min} = \frac{\pi^2 n^2 R_{L\min}}{8\eta_{tr}}\left(1 + \frac{r_{DS} + r_{LF}}{R_{L\min}} + \frac{2fQ_g V_{GSpp}}{P_{O\max}}\right) = \tag{B.5}$$

$$= \frac{\pi^2 0.25^2 200}{8 \times 0.98}\left(1 + \frac{0.02 + 0.02}{200} + \frac{2 \times 25300 \times 146 \times 10^{-9} \times 15}{5000}\right) = 15.74\Omega$$

The efficiency of the rectifier η_R,

$$\eta_R = \frac{\eta_{tr}}{1 + \frac{r_{DS} + r_{LF}}{R_{L\min}} + \frac{2fQ_g V_{GSpp}}{P_{O\max}}} \tag{B.6}$$

$$= \frac{0.98}{1 + \frac{0.02 + 0.02}{200} + \frac{2 \times 25300 \times 146 \times 10^{-9} \times 15}{5000}} = 0.98$$

The voltage transfer function of the rectifier can be found as follow,

$$\left|M_{VR}\right| = \frac{2\sqrt{2}\eta_{tr}}{\pi n \cdot \left(1 + \frac{r_{DS} + r_{LF}}{R_{L\min}} + \frac{2fQ_g V_{GSpp}}{P_{O\max}}\right)} \tag{B.7}$$

$$= \frac{2\sqrt{2} \times 0.98}{0.25\pi\left(1 + \frac{0.02 + 0.02}{200} + \frac{2 \times 25300 \times 146 \times 10^{-9} \times 15}{5000}\right)} = 3.53$$

The voltage transfer function of the converter,

$$M_V = \frac{V_O}{V_I} = \frac{1000}{250} = 4 \tag{B.8}$$

Assume $n = 0.25, \eta_{tr} = 0.98, \eta_I = 0.97$, $A = 1, Q_L = 2$ and $f_0 = 32.22kHz$, by solving (B.9) the normalized switching frequency can be calculated as $\frac{f}{f_0} = 0.7852$ and $f = 25.3kHz$.

$$M_V = \frac{8\eta_I \eta_{tr}}{n\pi^2 \sqrt{(1+A)^2\left[1-\left(\frac{f}{f_0}\right)^2\right]^2 + \left[\frac{1}{Q_L}\left(\frac{f}{f_0} - \frac{f_0}{f}\frac{A}{1+A}\right)\right]^2}} \tag{B.9}$$

The component values of the resonant circuit can be determined as follow,

$$L = \frac{R_{i\min}}{\omega_0 Q_L} = \frac{15.74}{2\pi \times 32220 \times 2} = 38.87\mu H \rightarrow 40\mu H \tag{B.10}$$

$$C = \frac{Q_L}{\omega_0 R_{i\min}} = \frac{2}{2\pi \times 32220 \times 15.74} = 0.63\mu F \tag{B.11}$$

$$C_1 = C \cdot \left(1 + \frac{1}{A}\right) = 2C = 1.26\mu F \rightarrow 1.2\mu F \tag{B.12}$$

$$C_2 = C \cdot (1+A) = 2C = 1.26\mu F \xrightarrow{on\ Transfomer\ Secondary} 0.082\mu F \tag{B.13}$$

Appendix C

Key Equations for LCC Resonant Network

This chapter summarizes the key equations developed by [17] in order to determine the LCC resonant tank characteristic.

$$X_s = \omega L_r - \frac{1}{\omega C_r} \tag{C.1}$$

$$X_p = -\frac{1}{\omega C_p} \tag{C.2}$$

$$Z_{i0} = jX_s \tag{C.3}$$

$$Z_{i\infty} = j\left(X_s + X_p\right) \tag{C.4}$$

$$H_\infty(\omega) = \frac{X_p}{X_s + X_p} \tag{C.5}$$

$$Z_{o0}(\omega) = \frac{jX_s X_p}{X_p + X_s} = jX_s H_\infty(\omega) \tag{C.6}$$

$$R_{crit} = \left| X_p \right| \sqrt{-\frac{X_s}{X_s + X_p}} \tag{C.7}$$

At $f = f_m$,

$$X_s = -\frac{1}{2} X_p \tag{C.8}$$

Output characteristic: $$\left(\frac{M}{a}\right)^2 + \left(\frac{J}{b}\right)^2 = 1 \tag{C.9}$$

Control characteristic: $$M = \frac{1}{\sqrt{\frac{1}{a^2} + \left(\frac{Q_e}{b}\right)^2}} \tag{C.10}$$

$$a = \left\| H_\infty(\omega) \right\| = \frac{\left\| X_p \right\|}{\left\| X_s + X_p \right\|} \tag{C.11}$$

$$b = \frac{\left\| H_\infty(\omega) \right\| R_o}{\left\| Z_{o0}(\omega) \right\|} = \frac{R_o}{\left| X_s \right|} \tag{C.12}$$

$$M = \frac{V_{out}}{V_{in}}, J = \frac{I_{out} R_o}{V_{in}}, Q_e = \frac{R_o}{R_e} \tag{C.13}$$

$$\omega_0 = \frac{1}{\sqrt{L_r C_r}}, \omega_\infty = \frac{1}{\sqrt{L_r C_r \parallel C_p}}, \omega_m = \frac{1}{\sqrt{L_r C_r \parallel 2C_p}} \tag{C.14}$$

Appendix D

Single Phase d-q Transformation

The d-q transformation requires both real and imaginary circuit. Although the imaginary orthogonal circuit does not exist, it can be constructed from the real components by applying 90° phase shift [6]. Figure D.1 shows the d-q reference frame where angle θ is the rotating angle of the d-q frame and it is defined by,

$$\theta = \int_0^t \omega(\tau) d\tau + \varphi \tag{D.1}$$

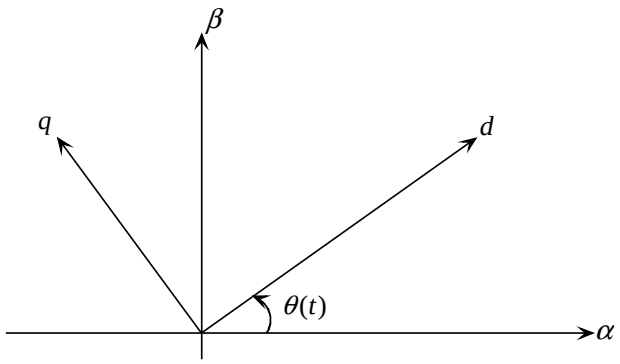

Figure D.1: The d-q reference frame

Single phase dq transformation:

$$X_R = X_m \cos(\omega t + \varphi) \tag{D.2}$$

$$X_I = X_m \sin(\omega t + \varphi) \tag{D.3}$$

Rotating transformation matrix,

$$T = \begin{bmatrix} \cos(\omega t) & \sin(\omega t) \\ -\sin(\omega t) & \cos(\omega t) \end{bmatrix} \tag{D.4}$$

$$T^{-1} = \begin{bmatrix} \cos(\omega t) & -\sin(\omega t) \\ \sin(\omega t) & \cos(\omega t) \end{bmatrix} \tag{D.5}$$

Applying the rotating transformation matrix (D.2) and (D.3),

$$\begin{bmatrix} X_d \\ X_q \end{bmatrix} = T \cdot \begin{bmatrix} X_R \\ X_I \end{bmatrix} = X_m \cdot \begin{bmatrix} \cos\varphi \\ \sin\varphi \end{bmatrix} \tag{D.6}$$

$$\begin{bmatrix} X_R \\ X_I \end{bmatrix} = T^{-1} \cdot \begin{bmatrix} X_d \\ X_q \end{bmatrix} \tag{D.7}$$

$$X_d + jX_q = X_m e^{j\varphi} \tag{D.8}$$

Appendix E

State Space Representation

The system equation is developed based on Figure 3.1.

$$V_{in} = L_r \frac{di_{Lr}}{dt} + R_r i_{Lr} + v_{Cr} + \frac{1}{n} v_{Cp} \tag{E.1}$$

$$\frac{1}{n} i_{Lr} = C_p \frac{dv_{Cp}}{dt} + i_R \tag{E.2}$$

$$i_{Lr} = C_r \frac{dv_{Cr}}{dt} \tag{E.3}$$

$$V_R = L_f \frac{di_f}{dt} + v_{out} \tag{E.4}$$

$$i_f = C_f \frac{dv_{out}}{dt} + \frac{v_{out}}{R_{load}} \tag{E.5}$$

where [2],

n is the transformer tap ratio

$$V_{in} = \frac{4}{\pi} V_{dc} \cos\varphi$$

$$i_R = \frac{4}{\pi} \frac{v_{Cp}}{\sqrt{V_{Cpd}^2 + V_{Cpq}^2}} i_f \quad \text{the current drawn by the rectifier}$$

$$V_R = \frac{2}{\pi} \sqrt{V_{Cpd}^2 + V_{Cpq}^2}$$

The system equations are converted into d-q frame using (D.4) as follow,

$$V_{in} = L_r \begin{bmatrix} 0 & \omega \\ -\omega & 0 \end{bmatrix} I_{Lrdq} + L_r \frac{dI_{Lrdq}}{dt} + R_r I_{Lrdq} + V_{Crdq} + \frac{1}{n} V_{Cpdq} \tag{E.6}$$

$$\frac{1}{n} I_{Lrdq} = C_p \begin{bmatrix} 0 & \omega \\ -\omega & 0 \end{bmatrix} V_{Cpdq} + C_p \frac{dV_{Cpdq}}{dt} + I_{Rdq} \tag{E.7}$$

$$I_{Lrdq} = C_r \begin{bmatrix} 0 & \omega \\ -\omega & 0 \end{bmatrix} V_{Crdq} + C_r \frac{dV_{Crdq}}{dt} \tag{E.8}$$

$$\begin{bmatrix} I_{Rd} \\ I_{Rq} \end{bmatrix} = \frac{4}{\pi} \frac{i_f}{\sqrt{V_{Cpd}^2 + V_{Cpq}^2}} \begin{bmatrix} V_{Cpd} \\ V_{Cpq} \end{bmatrix} \tag{E.9}$$

$$\frac{2}{\pi} \sqrt{V_{Cpd}^2 + V_{Cpq}^2} = L_f \frac{di_f}{dt} + v_{out} \tag{E.10}$$

$$i_f = C_f \frac{dv_{out}}{dt} + \frac{v_{out}}{R_{load}} \tag{E.11}$$

$$L_r \frac{dI_{Lrd}}{dt} = \frac{4}{\pi} V_{dc} \cos\varphi - \omega L_r I_{Lrq} - R_r I_{Lrd} - V_{Crd} - \frac{1}{n} V_{Cpd} \tag{E.12a}$$

$$L_r \frac{dI_{Lrq}}{dt} = \omega L_r I_{Lrd} - R_r I_{Lrq} - V_{Crq} - \frac{1}{n} V_{Cpq} \tag{E.12b}$$

$$C_p \frac{dV_{Cpd}}{dt} = \frac{1}{n} I_{Lrd} - \omega C_p V_{Cpq} - I_{Rd} \tag{E.13a}$$

$$C_p \frac{dV_{Cpq}}{dt} = \frac{1}{n} I_{Lrq} + \omega C_p V_{Cpd} - I_{Rq} \tag{E.13b}$$

$$I_{Lrd} = \omega C_r V_{Crq} + C_r \frac{dV_{Crd}}{dt} \tag{E.14}$$

$$I_{Lrq} = -\omega C_r V_{Crd} + C_r \frac{dV_{Crq}}{dt} \tag{E.15}$$

$$\begin{bmatrix} I_{Rd} \\ I_{Rq} \end{bmatrix} = \frac{4}{\pi} \frac{i_f}{\sqrt{V_{Cpd}^2 + V_{Cpq}^2}} \begin{bmatrix} V_{Cpd} \\ V_{Cpq} \end{bmatrix} \tag{E.16}$$

$$\frac{2}{\pi} \sqrt{V_{Cpd}^2 + V_{Cpq}^2} = L_f \frac{di_f}{dt} + v_{out} \tag{E.17}$$

$$i_f = C_f \frac{dv_{out}}{dt} + \frac{v_{out}}{R_{load}} \tag{E.18}$$

Combine (E.14), (E.15) and (E.16) with (E.12a), (E.12b), (E.13a) and (E.13b) to simplify the state equations into the following,

$$\frac{dI_{Lrd}}{dt} = \frac{1}{\left(L_r + \frac{1}{\omega^2 C_r} \right)} \cdot \left\{ -R_r I_{Lrd} - \left(\omega L_r - \frac{1}{\omega C_r} \right) I_{Lrq} - \frac{1}{n} V_{Cpd} + \frac{4}{\pi} V_{dc} \cos\varphi \right\} \tag{E.19a}$$

$$\frac{dI_{Lrq}}{dt} = \frac{1}{\left(L_r + \frac{1}{\omega^2 C_r} \right)} \cdot \left\{ -R_r I_{Lrq} + \left(\omega L_r - \frac{1}{\omega C_r} \right) I_{Lrd} - \frac{1}{n} V_{Cpq} \right\} \tag{E.19b}$$

$$\frac{dV_{Cpd}}{dt} = \frac{1}{C_p} \left\{ \frac{1}{n} I_{Lrd} - \omega C_p V_{Cpq} - \frac{4}{\pi} \frac{i_f}{\sqrt{V_{Cpd}^2 + V_{Cpq}^2}} V_{Cpd} \right\} \tag{E.20a}$$

$$\frac{dV_{Cpq}}{dt} = \frac{1}{C_p}\left\{\frac{1}{n} I_{Lrq} + \omega C_p V_{Cpd} - \frac{4}{\pi}\frac{i_f}{\sqrt{V_{Cpd}^2 + V_{Cpq}^2}} V_{Cpq}\right\} \tag{E.20b}$$

$$\frac{di_f}{dt} = \frac{1}{L_f}\left\{\frac{2}{\pi}\sqrt{V_{Cpd}^2 + V_{Cpq}^2} - v_{out}\right\} \tag{E.21}$$

$$\frac{dv_{out}}{dt} = \frac{1}{C_f}\left\{-\frac{v_{out}}{R_{load}} + i_f\right\} \tag{E.22}$$

The system operating point needs to be determining in order to linearize the system of equations around its operating point.

$$0 = -R_r I_{Lrd} - \left(\omega L_r - \frac{1}{\omega C_r}\right) I_{Lrq} - \frac{1}{n} V_{Cpd} + \frac{4}{\pi} V_{dc} \cos\varphi \tag{E.23}$$

$$0 = -R_r I_{Lrq} + \left(\omega L_r - \frac{1}{\omega C_r}\right) I_{Lrd} - \frac{1}{n} V_{Cpq} \tag{E.24}$$

$$0 = \frac{1}{n} I_{Lrd} - \omega C_p V_{Cpq} - \frac{4}{\pi}\frac{i_f}{\sqrt{V_{Cpd}^2 + V_{Cpq}^2}} V_{Cpd} \tag{E.25}$$

$$0 = \frac{1}{n} I_{Lrq} + \omega C_p V_{Cpd} - \frac{4}{\pi}\frac{i_f}{\sqrt{V_{Cpd}^2 + V_{Cpq}^2}} V_{Cpq} \tag{E.26}$$

$$0 = \frac{2}{\pi}\sqrt{V_{Cpd}^2 + V_{Cpq}^2} - v_{out} \tag{E.27}$$

$$0 = -\frac{v_{out}}{R_{load}} + i_f \tag{E.28}$$

$$I_f = \frac{V_{out}}{R_{load}} \tag{E.29}$$

$$V_{out} = \frac{2}{\pi}\sqrt{V_{Cpd}^2 + V_{Cpq}^2} \tag{E.30}$$

Equations (E.23) to (E.30) are simplified to develop a system of equation as follow,

$$I_{Lrd} = n\omega C_p V_{Cpq} + \frac{8n}{\pi^2}\frac{1}{R_{load}} V_{Cpd} \tag{E.31}$$

$$I_{Lrq} = \frac{8n}{\pi^2}\frac{1}{R_{load}} V_{Cpq} - n\omega C_p V_{Cpd} \tag{E.32}$$

$$\left(n\omega R_r C_p + \left(\omega L_r - \frac{1}{\omega C_r}\right)\cdot\frac{8n}{\pi^2}\frac{1}{R_{load}}\right)\cdot V_{Cpq} + \left(\frac{8n}{\pi^2}\frac{R_r}{R_{load}} - \left(\omega L_r - \frac{1}{\omega C_r}\right)\cdot n\omega C_p + \frac{1}{n}\right)\cdot V_{Cpd} = \frac{4}{\pi} V_{dc}\cos\varphi \tag{E.33}$$

$$-\left(\frac{8n}{\pi^2}\frac{R_r}{R_{load}} - \left(\omega L_r - \frac{1}{\omega C_r}\right)\cdot n\omega C_p + \frac{1}{n}\right)\cdot V_{Cpq} + \left(n\omega R_r C_p + \left(\omega L_r - \frac{1}{\omega C_r}\right)\frac{8n}{\pi^2}\frac{1}{R_{load}}\right)\cdot V_{Cpd} = 0 \tag{E.34}$$

Define,

$$\alpha = n\omega R_r C_p + \left(\omega L_r - \frac{1}{\omega C_r}\right)\cdot\frac{8n}{\pi^2}\frac{1}{R_{load}} \tag{E.25}$$

$$\beta = \frac{8n}{\pi^2}\frac{R_r}{R_{load}} - \left(\omega L_r - \frac{1}{\omega C_r}\right)\cdot n\omega C_p + \frac{1}{n} \tag{E.26}$$

$$\gamma = n\omega C_p \tag{E.27}$$

$$\sigma = \frac{8n}{\pi^2}\frac{1}{R_{load}} \tag{E.28}$$

The system operating points can be calculated as follows,

$$V_{Cpq0} = \frac{\alpha}{\alpha^2+\beta^2}\frac{4}{\pi} V_{dc}\cos\varphi_0 \tag{E.29}$$

$$V_{Cpd0} = \frac{\beta}{\alpha^2+\beta^2}\frac{4}{\pi} V_{dc}\cos\varphi_0 \tag{E.30}$$

$$I_{Lrd0} = \frac{\alpha\gamma+\beta\sigma}{\alpha^2+\beta^2}\frac{4}{\pi} V_{dc}\cos\varphi_0 \tag{E.31}$$

$$I_{Lrq0} = \frac{\alpha\sigma-\gamma\beta}{\alpha^2+\beta^2}\frac{4}{\pi} V_{dc}\cos\varphi_0 \tag{E.32}$$

$$I_{f0} = \frac{1}{\sqrt{\alpha^2 + \beta^2}} \frac{8}{\pi^2} \frac{1}{R_{load}} V_{dc} \cos\varphi_0 \tag{E.33}$$

Trim [34] describes the linearization of functions of one variable and multivariable functions around operating point can be determined as follow,

$$f(x) \approx f(c) + \left.\frac{df(x)}{dx}\right|_{x=c} (x-c) \tag{E.34}$$

$$f(x_1, x_2) \approx f(c,d) + \left.\frac{\partial f(x_1, x_2)}{\partial x_1}\right|_{x_1=c, x_2=d} (x_1 - c) + \left.\frac{\partial f(x_1, x_2)}{\partial x_2}\right|_{x_1=c, x_2=d} (x_2 - d) \tag{E.35}$$

The system of equations (E.19a) to (E.22) are linearized using (E.34) and (E.35) around the calculated operating points (E.29) to (E.33) as presented in (E.36) to (E.39).

$$f_1(\varphi) = \frac{\frac{4}{\pi} V_{dc} \cos\varphi}{\left(L_r + \frac{1}{\omega^2 C_r}\right)} \approx \frac{\frac{4}{\pi} V_{dc} \cos\varphi_0}{\left(L_r + \frac{1}{\omega^2 C_r}\right)} + \frac{-\frac{4}{\pi} V_{dc} \sin\varphi_0}{\left(L_r + \frac{1}{\omega^2 C_r}\right)} (\varphi - \varphi_0) \tag{E.36}$$

$$f_2(V_{Cpd}, V_{Cpq}) = \frac{2}{\pi L_f} \sqrt{V_{Cpd}^2 + V_{Cpq}^2} \tag{E.37}$$

$$\approx \frac{2}{\pi L_f} \frac{V_{Cpd\,0}}{\sqrt{V_{Cpd\,0}^2 + V_{Cpq\,0}^2}} V_{Cpd} + \frac{2}{\pi L_f} \frac{V_{Cpq\,0}}{\sqrt{V_{Cpd\,0}^2 + V_{Cpq\,0}^2}} V_{Cpq}$$

$$f_3(I_f, V_{Cpd}, V_{Cpq}) = -\frac{4}{\pi C_p} \frac{I_f}{\sqrt{V_{Cpd}^2 + V_{Cpq}^2}} V_{Cpd} \tag{E.38}$$

$$\approx -\frac{4}{\pi C_p} \frac{V_{Cpd\,0}}{\sqrt{V_{Cpd\,0}^2 + V_{Cpq0}^2}} I_f$$
$$+ \left(-\frac{4}{\pi C_p} \frac{I_{f0}}{\sqrt{V_{Cpd\,0}^2 + V_{Cpq0}^2}} + \frac{4}{\pi C_p} \frac{I_{f0} V_{Cpd\,0}^2}{\left(V_{Cpd\,0}^2 + V_{Cpq0}^2\right)^{3/2}} \right) \cdot V_{Cpd} + \frac{4}{\pi C_p} \frac{I_{f0} V_{Cpd\,0} V_{Cpq0}}{\left(V_{Cpd\,0}^2 + V_{Cpq0}^2\right)^{3/2}} V_{Cpq}$$
$$+ \left(\frac{4}{\pi C_p} \frac{I_{f0} V_{Cpd\,0}}{\sqrt{V_{Cpd\,0}^2 + V_{Cpq0}^2}} - \frac{4}{\pi C_p} \frac{I_{f0} V_{Cpd\,0}^3}{\left(V_{Cpd\,0}^2 + V_{Cpq0}^2\right)^{3/2}} + \frac{4}{\pi C_p} \frac{I_{f0} V_{Cpd\,0} V_{Cpq0}^2}{\left(V_{Cpd\,0}^2 + V_{Cpq0}^2\right)^{3/2}} \right)$$

$$f_4\left(I_f, V_{Cpd}, V_{Cpq}\right) = -\frac{4}{\pi C_p}\frac{I_f}{\sqrt{V_{Cpd}^2 + V_{Cpq}^2}}V_{Cpq} \tag{E.39}$$

$$\approx -\frac{4}{\pi C_p}\frac{V_{Cpq0}}{\sqrt{V_{Cpd0}^2 + V_{Cpq0}^2}}I_f$$
$$+\left(-\frac{4}{\pi C_p}\frac{I_{f0}}{\sqrt{V_{Cpd0}^2 + V_{Cpq0}^2}} + \frac{4}{\pi C_p}\frac{I_{f0}V_{Cpq0}^2}{\left(V_{Cpd0}^2 + V_{Cpq0}^2\right)^{3/2}}\right)\cdot V_{Cpq} + \frac{4}{\pi C_p}\frac{I_{f0}V_{Cpd0}V_{Cpq0}}{\left(V_{Cpd0}^2 + V_{Cpq0}^2\right)^{3/2}}V_{Cpd}$$
$$+\left(\frac{4}{\pi C_p}\frac{I_{f0}V_{Cpq0}}{\sqrt{V_{Cpd0}^2 + V_{Cpq0}^2}} - \frac{4}{\pi C_p}\frac{I_{f0}V_{Cpq0}^3}{\left(V_{Cpd0}^2 + V_{Cpq0}^2\right)^{3/2}} + \frac{4}{\pi C_p}\frac{I_{f0}V_{Cpq0}V_{Cpd0}^2}{\left(V_{Cpd0}^2 + V_{Cpq0}^2\right)^{3/2}}\right)$$

By replacing (3.36) to (3.39) into (E.19a) to (E.22), the state space representation of the DC/DC resonant converter is determined as follow,

$$X = \begin{bmatrix} I_{Lrd} \\ I_{Lrq} \\ V_{Cpd} \\ V_{Cpq} \\ I_f \\ V_{out} \end{bmatrix} \tag{E.40}$$

$$Y = V_{out} \tag{E.41}$$

$$U = [\varphi] \tag{E.42}$$

$$B = \begin{bmatrix} \dfrac{-\dfrac{4}{\pi}V_{dc}\sin\varphi_0}{\left(L_r + \dfrac{1}{\omega^2 C_r}\right)} \\ 0 \\ 0 \\ 0 \\ 0 \\ 0 \end{bmatrix} \tag{E.43}$$

$$C = \begin{bmatrix} 0 & 0 & 0 & 0 & 0 & 1 \end{bmatrix} \tag{E.44}$$

$$A=\begin{bmatrix}
\dfrac{-R_r}{L_r+\dfrac{1}{\omega^2 C_r}} & \dfrac{-\left(\omega L_r-\dfrac{1}{\omega C_r}\right)}{L_r+\dfrac{1}{\omega^2 C_r}} & \dfrac{-1}{\left(L_r+\dfrac{1}{\omega^2 C_r}\right)\cdot n} & 0 & 0 & 0 \\
\dfrac{\left(\omega L_r-\dfrac{1}{\omega C_r}\right)}{L_r+\dfrac{1}{\omega^2 C_r}} & \dfrac{-R_r}{L_r+\dfrac{1}{\omega^2 C_r}} & 0 & \dfrac{-1}{\left(L_r+\dfrac{1}{\omega^2 C_r}\right)\cdot n} & 0 & 0 \\
\dfrac{1}{nC_p} & 0 & -\dfrac{4}{\pi C_p}\dfrac{I_{f0}}{\sqrt{V_{Cpd0}^2+V_{Cpq0}^2}}+\dfrac{4}{\pi C_p}\dfrac{I_{f0}V_{Cpd0}^2}{\left(V_{Cpd0}^2+V_{Cpq0}^2\right)^{3/2}} & -\omega+\dfrac{4}{\pi C_p}\dfrac{I_{f0}V_{Cpd0}V_{Cpq0}}{\left(V_{Cpd0}^2+V_{Cpq0}^2\right)^{3/2}} & -\dfrac{4}{\pi C_p}\dfrac{V_{Cpd0}}{\sqrt{V_{Cpd0}^2+V_{Cpq0}^2}} & 0 \\
0 & \dfrac{1}{nC_p} & \omega+\dfrac{4}{\pi C_p}\dfrac{I_{f0}V_{Cpd0}V_{Cpq0}}{\left(V_{Cpd0}^2+V_{Cpq0}^2\right)^{3/2}} & -\dfrac{4}{\pi C_p}\dfrac{I_{f0}}{\sqrt{V_{Cpd0}^2+V_{Cpq0}^2}}+\dfrac{4}{\pi C_p}\dfrac{I_{f0}V_{Cpq0}^2}{\left(V_{Cpd0}^2+V_{Cpq0}^2\right)^{3/2}} & -\dfrac{4}{\pi C_p}\dfrac{V_{Cpq0}}{\sqrt{V_{Cpd0}^2+V_{Cpq0}^2}} & 0 \\
0 & 0 & \dfrac{2}{\pi L_f}\dfrac{V_{Cpd0}}{\sqrt{V_{Cpd0}^2+V_{Cpq0}^2}} & \dfrac{2}{\pi L_f}\dfrac{V_{Cpq0}}{\sqrt{V_{Cpd0}^2+V_{Cpq0}^2}} & 0 & \dfrac{-1}{L_f} \\
0 & 0 & 0 & 0 & \dfrac{1}{C_f} & \dfrac{-1}{R_{load}C_f}
\end{bmatrix}$$

Appendix F

DC/DC Resonant Converter Average Model

Sanders [31] proved the following mathematical relationships,

$$sign(x) = \begin{cases} 1 & x > 0 \\ 0 & x = 0 \\ -1 & x < 0 \end{cases} \tag{F.1}$$

$$\langle sign(x) \rangle_0 = 0 \tag{F.2}$$

$$\langle sign(x) \rangle_1 = \frac{2}{\pi} e^{j\angle\langle x\rangle_1} \tag{F.3}$$

$$\langle abs(x) \rangle_0 = \frac{4}{\pi} \left\| \langle x \rangle_1 \right\| \tag{F.4}$$

$$\langle abs(x) \rangle_1 = 0 \tag{F.5}$$

Convert (4.9) to (4.12) into complex Form using (4.3) and (4.4).

$$\frac{d}{dt}\langle i_{Lr} \rangle_k = -jk\omega \langle i_{Lr} \rangle_k + \frac{1}{L_r}\left(\langle V_d \rangle_k - R_r \langle i_{Lr} \rangle_k - \langle v_{Cr} \rangle_k - \frac{1}{n} \langle v_{out} \cdot sign(i_{Lr}) \rangle_k \right) \tag{F.6}$$

$$\frac{d}{dt}\langle v_{Cr}\rangle_k = -jk\omega\langle v_{Cr}\rangle_k + \frac{1}{C_r}\langle i_{Lr}\rangle_k \tag{F.7}$$

$$\frac{d}{dt}\langle v_{out}\rangle_k = -jk\omega\langle v_{out}\rangle_k + \frac{1}{C_f}\left(\frac{1}{n}\langle abs(i_{Lr})\rangle_k - \frac{1}{R_{load}}\langle v_{out}\rangle_k\right) \tag{F.8}$$

where,

$$\langle i_{Lr}\rangle_1 = x_1 + jx_2 \tag{F.9}$$

$$\langle v_{Cr}\rangle_1 = x_3 + jx_4 \tag{F.10}$$

$$\langle v_{out}\rangle_1 = x_5 + jx_6 \tag{F.11}$$

For $k = 0$, the DC components:

$$\frac{d}{dt}\langle i_{Lr}\rangle_0 = \frac{1}{L_r}\left(-R_r\langle i_{Lr}\rangle_0 - \langle v_{Cr}\rangle_0\right) \tag{F.12}$$

$$\frac{d}{dt}\langle v_{Cr}\rangle_0 = \frac{1}{C_r}\langle i_{Lr}\rangle_0 \tag{F.13}$$

$$\frac{d}{dt}\langle v_{out}\rangle_0 = \frac{1}{C_f}\left(\frac{4}{n\pi}\sqrt{x_1^2 + x_2^2} - \frac{1}{R_{load}}\langle v_{out}\rangle_0\right) \tag{F.14}$$

For $k = 1$, the first harmonic:

$$\frac{d}{dt}\langle i_{Lr}\rangle_1 = -j\omega\langle i_{Lr}\rangle_1 + \frac{1}{L_r}\left(\langle V_d\rangle_1 - R_r\langle i_{Lr}\rangle_1 - \langle v_{Cr}\rangle_1 - \frac{1}{n}\left\{\langle v_{out}\rangle_1\langle sign(i_{Lr})\rangle_0 + \langle v_{out}\rangle_0\langle sign(i_{Lr})\rangle_1\right\}\right) \tag{F.15}$$

$$\frac{d}{dt}\langle v_{Cr}\rangle_1 = -j\omega\langle v_{Cr}\rangle_1 + \frac{1}{C_r}\langle i_{Lr}\rangle_1 \tag{F.16}$$

$$\frac{d}{dt}\langle v_{out}\rangle_1 = -j\omega\langle v_{out}\rangle_1 + \frac{1}{C_f}\left(\frac{1}{n}\langle abs(i_{Lr})\rangle_1 - \frac{1}{R_{load}}\langle v_{out}\rangle_1\right) \tag{F.17}$$

$$\frac{d}{dt}\langle i_{Lr}\rangle_1 = -j\omega\langle i_{Lr}\rangle_1 + \frac{1}{L_r}\left(-j\frac{2}{\pi}V_{dc} - R_r\langle i_{Lr}\rangle_1 - \langle v_{Cr}\rangle_1 - \frac{2}{n\pi}\langle v_{out}\rangle_0 e^{j\langle i_{Lr}\rangle_1}\right) \tag{F.18}$$

$$\frac{d}{dt}\langle v_{Cr}\rangle_1 = -j\omega\langle v_{Cr}\rangle_1 + \frac{1}{C_r}\langle i_{Lr}\rangle_1 \tag{F.19}$$

$$\frac{d}{dt}\langle v_{out}\rangle_1 = -j\omega\langle v_{out}\rangle_1 - \frac{1}{C_f R_{load}}\langle v_{out}\rangle_1 \tag{F.20}$$

where,

$$\varphi = \tan^{-1}\left(\frac{x_2}{x_1}\right) \tag{F.21}$$

$$\frac{d}{dt}x_1 = \omega\cdot x_2 + \frac{1}{L_r}\left(-R_r\cdot x_1 - x_3 - \frac{2}{n\pi}\langle v_{out}\rangle_0\cos\varphi\right) \tag{F.22}$$

$$\frac{d}{dt}x_2 = -\omega\cdot x_1 + \frac{1}{L_r}\left(-\frac{2}{\pi}V_{dc} - R_r\cdot x_2 - x_4 - \frac{2}{n\pi}\langle v_{out}\rangle_0\sin\varphi\right) \tag{F.23}$$

$$\frac{d}{dt}x_3 = \omega\cdot x_4 + \frac{1}{C_r}x_1 \tag{F.24}$$

$$\frac{d}{dt}x_4 = -\omega\cdot x_3 + \frac{1}{C_r}x_2 \tag{F.25}$$

$$\frac{d}{dt}x_5 = \omega\cdot x_6 - \frac{1}{C_f R_{load}}x_5 \tag{F.26}$$

$$\frac{d}{dt}x_6 = -\omega\cdot x_5 - \frac{1}{C_f R_{load}}x_6 \tag{F.27}$$

$$i_{Lr}(t) = \langle i_{Lr}\rangle_{-1}e^{-j\omega t} + \langle i_{Lr}\rangle_0 + \langle i_{Lr}\rangle_1 e^{j\omega t} = 2x_1\cos\omega t + \langle i_{Lr}\rangle_0 + 2x_2\sin\omega t \tag{F.28}$$

$$v_{Cr}(t) = \langle v_{Cr}\rangle_{-1}e^{-j\omega t} + \langle v_{Cr}\rangle_0 + \langle v_{Cr}\rangle_1 e^{j\omega t} = 2x_3\cos\omega t + \langle v_{Cr}\rangle_0 + 2x_4\sin\omega t \tag{F.29}$$

$$v_{out}(t) = \langle v_{out}\rangle_{-1}e^{-j\omega t} + \langle v_{out}\rangle_0 + \langle v_{out}\rangle_1 e^{j\omega t} = 2x_5\cos\omega t + \langle v_{out}\rangle_0 + 2x_6\sin\omega t \tag{F.30}$$